

第 15 回
核燃焼プラズマ
統合コード研究会

**15th Burning Plasma Simulation
Initiative (BPSI) Meeting**

日時：2017年11月29日(水)–30日(木)
場所：九州大学筑紫キャンパス
応用力学研究所 2階大会議室



第 15 回核燃焼プラズマ統合コード研究会

15th Burning Plasma Simulation Initiative (BPSI) Meeting

(Ver.2)

日時：2017年11月29日(水)–30日(木)

場所：九州大学筑紫キャンパス 応用力学研究所 2階大会議室

(18 min talk+7 min discuss or (15 or 10) min talk+5min discuss)

11月29日(水)

9:30 – 9:40 はじめに 村上 (京大)

9:40 – 9:45 事務連絡 糟谷 (九大)

(座長：糟谷)

9:45 – 10:10 講演 1-1 登田 (核融合研)

Reduced models for electron and ion heat diffusivities by gyro-kinetic analysis with kinetic electrons in helical plasmas

10:10 – 10:35 講演 1-2 山口 (核融合研)

Integrated transport simulation of LHD plasmas with transport models based on GK simulations and experiment database

10:35 – 10:55 休憩

10:55 – 11:20 講演 1-3 村上 (京大)

Simulation study of fusion reaction rate and comparison with experimental results in LHD

11:20 – 11:40 講演 1-4 前田 (京大)

Integrated transport simulation of LHD plasma by TASK3D

11:40 – 11:55 講演 1-5 山本 (京大)

Effects of electron cyclotron heating on the toroidal flow in helical plasmas

11:55 – 13:00 昼休み

(座長：本多)

13:00 – 13:25 講演 2-1 滝塚 (阪大)

PARASOL simulation of ELM heat flux in tokamak SOL-divertor plasma

13:25 – 13:50 講演 2-2 東郷 (筑波大)、代理発表 滝塚

Effect of parallel viscosity approximation in inhomogeneous magnetic fields on SOL-divertor plasma profiles

13:50 – 14:15 講演 2-3 伊庭野 (阪大)
Simulation of vapor shielding at a solid wall by a weighted PIC method

14:15 – 14:40 講演 2-4 大澤 (九大)
Simulation for stability of di-vacancy in tungsten

14:40 – 15:00 休憩

(座長 : 福山)

15:00 – 15:25 講演 2-5 本多 (量研機構)
Application of genetic algorithms to modelings of plasma physics

15:25 – 15:50 講演 2-6 Hahm (Seoul Univ.)
Effects of 3D compressional magnetic fields on zonal flows in tokamak plasmas

15:50 – 16:15 講演 2-7 小菅 (九大)
Pattern selection in drift wave turbulence with parallel flows

16:15 – 16:40 講演 2-8 佐々木 (九大)
Suppression and enhancement of turbulence by geodesic acoustic modes

16:40 – 16:55 講演 2-9 大野 (九大)
Analysis of parameter dependency of ion-temperature-gradient instability using a gyro-fluid model in linear devices

16:55 散会

19:00 – 22:00 懇親会 (博多前炉ばた 一承にて)

11月30日(木)

9:30 – 9:35 事務連絡

(座長：村上)

9:35 – 10:00 講演 3-1 福山 (京大)

Progress in development of module interface of integrated code

10:00 – 10:25 講演 3-2 糟谷 (九大)

On effects of impurity and neutral in magnetically confined plasmas

10:25 – 10:45 休憩

10:45 – 11:10 講演 3-3 沼波 (核融合研)

Simulation studies on transport of multi-species plasmas including impurity ion

11:10 – 11:35 講演 3-4 矢木 (量研機構)

Simulation study on internal transport barrier formation using gyro fluid model (II)

11:35 – 11:50 まとめと議論 糟谷 (九大)

Summary and discussion

11:50 – 13:00 昼休み

13:00 – 17:00 核融合エネルギーフォーラムサブクラスター会合

17:00 散会

Reduced models for electron and ion heat diffusivities by gyro-kinetic analysis with kinetic electrons in helical plasmas

S. Toda, M. Nakata, M. Nunami, A. Ishizawa¹, T. -H. Watanabe² and H. Sugama

National Institute for Fusion Science, Oroshi-cho 322-6, Toki, Gifu, 509-5292, Japan

¹*Graduate School of Energy Science, Kyoto Uni., Gokasho, Uji, Kyoto, 611-0011, Japan*

²*Department of Physics, Nagoya University, Furo-cho, Nagoya, Aichi, 464-8602, Japan*

Turbulent transport is one of the most critical issues for plasma confinement in magnetic fusion devices. A large number of the gyro-kinetic simulations which are applied to the turbulent transport have been performed in toroidal plasmas. The gyro-kinetic analysis results in tokamak and helical plasmas have been studied with the experimental observations. Gyro-kinetic simulations of helical plasmas require a large number of mesh points along the field line in order to capture the helical ripple structure. Therefore, the gyro-kinetic analysis in helical plasmas consumes the larger computer resources than for tokamaks. The reduced model, which reproduces the nonlinear gyro-kinetic analysis results, is needed for the transport simulation in helical plasmas.

The GKV code [1] has been used to examine the ion temperature gradient (ITG) mode and zonal flows in the Large Helical Device (LHD) for studying the turbulent transport. The gyro-kinetic simulation with the adiabatic electron is performed for the high ion temperature LHD discharge (shot number 88343 [2]). The ion energy flux by the ITG mode instability agrees with the experimental results for the high- T_i plasmas at $t = 2.2$ s in the high- T_i LHD discharge #88343 [3]. The reduced model for the ion heat diffusivity is proposed [3] by the simulation with the adiabatic electron. This reduced model is the function of the linear growth rate for the ITG mode and the zonal flow decay time [4]. How to apply the reduced model of the turbulent ion heat diffusivity from the gyro-kinetic simulation with the adiabatic electron to the transport code has been shown in helical plasmas [5]. The simulation with the kinetic electron shows the larger ion energy flux than the experimental results in the high- T_i plasmas [6]. On the other hand, the electron and ion energy fluxes of the simulation results with the kinetic electron are close to those of the experimental results in the low- T_i #88343 plasmas [7] at $t = 1.9$ s in the LHD discharge #88343. To show the reduced transport model for the turbulent electron and ion heat diffusivities, the effect of the kinetic electron on the plasma instability has been included. If the small number for the wave-length is taken, the reduced model for the ion heat diffusivity was proposed. At that time, the electromagnetic part in the total electron heat flux becomes large around 30%, in spite of the low beta plasma studied [8]. In this study, the reduced models of the electron and ion heat diffusivities for the ITG mode are proposed by solving the gyro-kinetic equation in terms of the electron in addition to the ion to examine the effect of the kinetic electron. The similar method with the gyro-kinetic analysis using the adiabatic electron [3] is adopted. The nonlinear gyro-kinetic simulation is performed to evaluate the electron and ion heat diffusivities, when the number of the wave-length taken in the simulation is larger than the study to estimate only the ion heat diffusivity [8]. The effect of the kinetic electron on the linear response of zonal flows is studied. The linear gyro-kinetic simulation is also performed for the reduced model in order to reproduce the values of the heat diffusivities by the nonlinear analysis.

The turbulence driven by the microinstabilities is studied in LHD plasmas, using the gyro-kinetic local flux tube code GKV [1]. Based on the temperatures radial profiles, density radial profiles, and field configuration from the LHD experimental results of the high- T_i plasmas at $t = 2.2$ s and of the low- T_i plasmas at $t = 1.8$ s, 1.9s [2], the electron and ion temperature gradients, R/L_{T_e} and R/L_{T_i} , the density gradient R/L_n , and the safety factor q radially change. The GKV simulation

with the kinetic electrons is performed for the three dimensional equilibrium field configurations with $R = 3.75\text{m}$ for the high- T_i plasmas and with $R = 3.6\text{m}$ for the low- T_i plasmas. The β value is 0.3% at $\rho = 0.65$ for the high- T_i plasmas. To reduce the electromagnetic part in electron energy flux and the particle flux, we take the larger number for the Fourier modes and the larger number of the grid points for the parallel direction in this simulation than in the study [8]. The total Fourier mode numbers in the \tilde{k}_x and \tilde{k}_y directions are 41 and 12, where \tilde{k}_x and \tilde{k}_y are the radial and poloidal wavenumbers. The total grid number in the parallel direction, the parallel velocity direction and the perpendicular velocity direction are 512, 64 and 16. In the high- T_i plasmas, the nonlinear GKV simulations are performed at ten radial points between $\rho = 0.46$ and $\rho = 0.80$. The nonlinear simulations are also carried out at the ten radial points between $\rho = 0.65$ and $\rho = 0.80$ in the low- T_i plasmas. The time evolution of the electron and ion energy fluxes, and the particle flux at $\rho = 0.68$ for the high- T_i plasmas is examined. The saturation of the electron and ion energy fluxes and the particle flux is obtained in the nonlinear phase. The temporal traces for the ratio of the electromagnetic contributions Q_e^{em} , Q_i^{em} and Γ^{em} to the electron and ion energy flux Q_e , Q_i and the particle flux Γ are examined. The time averaged values of Q_e^{em}/Q_e , Q_i^{em}/Q_i and Γ^{em}/Γ are 6.3%, -0.76% and 8.1% at the low- β plasma ($\simeq 0.3\%$) case. Because the larger number of the modes is taken, the ratio of the electromagnetic part to the electron energy flux significantly becomes smaller than the simulation result [8]. The averaged values of the electron and ion energy flux at $\rho = 0.65$ in the time interval $50 < t < 100$ for the high- T_i plasmas are 0.036 MW/m^2 and 0.11 MW/m^2 . The time averaged value of the particle flux is around $-1.0 \times 10^{19}/(\text{m}^2\text{s})$. In the simulation results [6], the averaged values of the electron and ion energy flux in the time interval $50 < t < 80$ are about 0.046 MW/m^2 and 0.13 MW/m^2 , when the Fourier mode numbers in the \tilde{k}_x and \tilde{k}_y directions are 169 and 43. The time averaged value of the particle flux is around $-1.0 \times 10^{19}/(\text{m}^2\text{s})$. Even if the number of the Fourier modes is smaller than the simulation results [6], the close values of the electron and ion energy flux and the particle flux are obtained in this study. The time evolutions of the squared turbulent potential fluctuation, $\mathcal{T} \left(= \sum_{\tilde{k}_x, \tilde{k}_y \neq 0} \left\langle \left| \tilde{\phi}_{\tilde{k}_x, \tilde{k}_y} \right|^2 \right\rangle / 2 \right)$ and the squared zonal flow potential, $\mathcal{Z} \left(= \sum_{\tilde{k}_x} \left\langle \left| \tilde{\phi}_{\tilde{k}_x, \tilde{k}_y=0} \right|^2 \right\rangle / 2 \right)$ are studied. The nonlinear saturation is seen in the time evolution of \mathcal{T} and \mathcal{Z} .

The nominal values of the LHD experimental results at $t = 2.2\text{s}$ for high- T_i plasmas and at $t = 1.8\text{s}, 1.9\text{s}$ for the low- T_i plasmas are used. The radial profiles of the electron and ion energy flux, and the particle flux are examined as the nonlinear simulation results. In this study, the reduced model of the particle diffusivity is not shown, because the stationary condition of the turbulent particle flux with the neoclassical flux with no particle source is violated at $\rho < 0.5$ in the high- T_i plasmas and in the low- T_i plasmas [7]. The transport coefficients $\bar{\chi}_e/\chi_i^{GB}$ and $\bar{\chi}_i/\chi_i^{GB}$ by the nonlinear simulation are compared with model functions of $\bar{\mathcal{T}}$ and $\bar{\mathcal{Z}}$, where the bar represents the averaged value in the time interval of the nonlinear saturation phase. A fitting function for the electron heat diffusivity is defined by $\bar{\chi}_e/\chi_i^{GB} = \mathcal{F}_e(\bar{\mathcal{T}}, \bar{\mathcal{Z}}) \equiv C_{1e}\bar{\mathcal{T}}^{\alpha_e}/(C_{2e} + \bar{\mathcal{Z}}^\xi/\bar{\mathcal{T}})$ with $\alpha_e = 0.19$, $C_{1e} = 6.8 \times 10^{-2}$, $C_{2e} = 2.1 \times 10^{-2}$ and $\xi = 0.10$, where χ_i^{GB} is the gyro-Bohm diffusivity. The relative error for fitting $\bar{\chi}_e/\chi_i^{GB}$ by \mathcal{F}_e is 0.079, where the relative error is defined as the root mean square of $[(\bar{\chi}_e/\chi_i^{GB})/\mathcal{F}_e - 1]$. A fitting function for the ion heat diffusivity is also defined by $\bar{\chi}_i/\chi_i^{GB} = \mathcal{F}_i(\bar{\mathcal{T}}, \bar{\mathcal{Z}}) \equiv C_{1i}\bar{\mathcal{T}}^{\alpha_i}/(C_{2i} + \bar{\mathcal{Z}}^{\frac{1}{2}}/\bar{\mathcal{T}})$ with $\alpha_i = 0.41$, $C_{1i} = 0.13$ and $C_{2i} = 4.9 \times 10^{-2}$. The relative error for fitting $\bar{\chi}_i/\chi_i^{GB}$ by \mathcal{F}_i is 0.15. The exponent of \mathcal{Z} in \mathcal{F}_i is found to be larger than that in \mathcal{F}_e , therefore the effect of zonal flows in χ_i is stronger than that in χ_e . The values of the electron and ion heat diffusivities are well reproduced by the model functions.

To represent the contributions of the turbulent fluctuations and zonal flow fluctuations to the turbulence level by the linear gyro-kinetic analysis, the simulation is performed with the kinetic electron. The radial profiles the mixing length estimate \mathcal{L} ($\equiv \int (\tilde{\gamma}_{\tilde{k}_y} / \tilde{k}_y^2) d\tilde{k}_y$) typically integrated over $0.05 \leq \tilde{k}_y \leq 0.1$ with the adiabatic and the kinetic electrons are studied for the high- T_i plasmas, where $\tilde{\gamma}_{\tilde{k}_y}$ is the linear growth rate. The turbulence fluctuation $\bar{\mathcal{T}}$ is approximated by $\bar{\mathcal{T}} = C_T \mathcal{L}^a$ with the coefficients $C_T = 6.6 \times 10$ and $a = 1.6$. The level of the turbulence is determined by the interaction between the turbulence and the zonal flows. The linear zonal flow response function is defined by $\mathcal{R}_{\tilde{k}_x}(t) \equiv \langle \tilde{\phi}_{\tilde{k}_x, \tilde{k}_y=0}(t) \rangle / \langle \tilde{\phi}_{\tilde{k}_x, \tilde{k}_y=0}(t=0) \rangle$. The linear zonal flow response is examined using the field configuration for the high- T_i and low- T_i phases in the LHD #88343 discharge. Note that we set the value of \tilde{k}_x around 0.25, because there is a peak of the wavenumber spectra around $\tilde{k}_x = 0.25$ as the results of the nonlinear simulation. The zonal flow decay time is defined by $\tau_{ZF} \equiv \int_0^{\tau_f} dt \mathcal{R}_{\tilde{k}_x}(t)$. Here, we set $\tau_f = 30R/v_{ti}$, because the zonal flow decay time does not change significantly for $\tau_f > 30R/v_{ti}$. The correlation time of the turbulence in the nonlinear simulation result is shorter than $30R/v_{ti}$, thus $\mathcal{R}_{\tilde{k}_x}(t)$ for $\tau_f > 30R/v_{ti}$ does not influence the excited zonal flow level. The zonal flow fluctuation $\bar{\mathcal{Z}}$ is approximated by the linear simulation results with the relation, $\bar{\mathcal{Z}}^b / \bar{\mathcal{T}}^c = C_z \tilde{\tau}_{ZF}$ with $C_z = 0.91$, $b = 0.16$ and $c = 0.27$.

The reduced models which represent the electron and ion heat diffusivities in terms of the linear plasma parameters by the simulation with the kinetic electron are shown as $\chi_e^{RM} / \chi_i^{GB} = A_{1e} \mathcal{L}^{B_{1e}} / (A_{2e} + \tilde{\tau}_{ZF}^{B_{2e}} / \mathcal{L}^{B_{3e}})$, and $\chi_i^{RM} / \chi_i^{GB} = A_{1i} \mathcal{L}^{B_{1i}} / (A_{2i} + \tilde{\tau}_{ZF}^{B_{2i}} / \mathcal{L}^{B_{3i}})$, where the coefficients are given by $A_{1e} = C_{1e} C_T^{\alpha_e + 1 - c\xi/b} C_z^{-\xi/b} = 1.3 \times 10$, $A_{2e} = C_{2e} C_T^{1 - c\xi/b} C_z^{-\xi/b} = 2.0$, $A_{1i} = C_{1i} C_T^{\alpha_i + 1 - c/(2b)} C_z^{-1/(2b)} = 2.6 \times 10^2$ and $A_{2i} = C_{2i} C_T^{1 - c/(2b)} C_z^{-1/(2b)} = 1.8 \times 10$. The exponents are given by $B_{1e} = \alpha_e a = 0.30$, $B_{2e} = \xi/b = 0.62$, and $B_{3e} = a(1 - c\xi/b) = 0.63$, $B_{1i} = \alpha_i a = 0.66$, $B_{2i} = 1/(2b) = 3.1$ and $B_{3i} = a(1 - c/(2b)) = 0.26$. By the linear gyro-kinetic simulation, the values of χ_e^{RM} and χ_i^{RM} are obtained. The electron diffusivity χ_e^{RM} and $\bar{\chi}_e$ are compared in Fig. 1(a) and the ion diffusivity χ_i^{RM} and $\bar{\chi}_i$ are also compared in Fig. 1(b). The circles and the boxes show the results in high- T_i and low- T_i phases. The reduced models reproduces the nonlinear simulation results $\bar{\chi}_e$ for the relative error 0.21 and $\bar{\chi}_i$ for the relative error 0.20.

This work was partly supported by the NIFS Collaboration Research programs (Plasma Simulator), NIFS16KNST093, NIFS16KNTT035 and the Collaborative Research Program of Research Institute for Applied Mechanics, Kyushu University, 29FP-4.

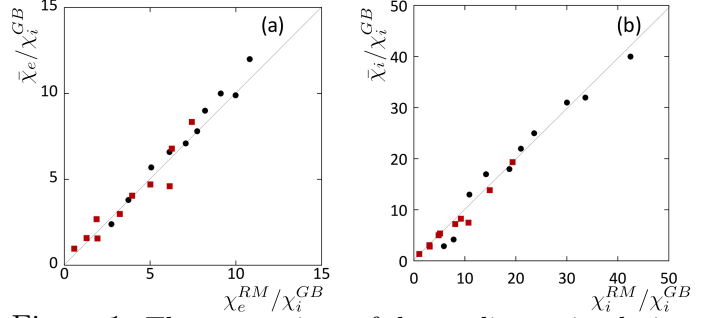


Figure 1: The comparison of the nonlinear simulation results, $\bar{\chi}_e$ and $\bar{\chi}_i$ with the model predictions.

- [1] T. -H. Watanabe and H. Sugama *Nucl. Fusion* **46**, 24 (2006)
- [2] K. Tanaka, et al., *Plasma and Fusion Research* **5**, S2053 (2010)
- [3] M. Nunami, T. -H. Watanabe and H. Sugama, *Phys. Plasmas* **20**, 092307 (2013)
- [4] H. Sugama and T. -H. Watanabe, *Phys. Plasmas* **13**, 012501 (2006)
- [5] S. Toda et al., *Journal of Physics: Conference Series* **561**, 012020 (2014)
- [6] A. Ishizawa et al., *Nucl. Fusion* **55**, 043024 (2015)
- [7] A. Ishizawa et al., *Nucl. Fusion* **57**, 066010 (2017)
- [8] S. Toda et al., *Plasma and Fusion Research* **12**, 1303035 (2017)

Study of Energetic Particle Confinement by Triton Burn-up Experiment in LHD

S. Murakami¹, M. Isobe^{2,3}, K. Ogawa^{2,3}, T. Nishitani², S. Kamio², Y. Fujiwara², N. Pu³, H. Kawase³, M. Osakabe^{2,3}, Y. Saito¹, S. Maeta¹, H. Yamaguchi², LHD Exp group²

¹*Department of Nuclear Engineering, Kyoto University,*

²*National Institute for Fusion Science, National Institutes of Natural Sciences*

³*School of Physical Sciences, SOKENDAI (The Graduate University for Advanced Studies)*

e-mail: murakami@nucleng.kyoto-u.ac.jp

The energetic particle confinement is investigated by triton burn-up experiment in LHD. A significant increase of triton burn-up ratio can be seen in the strongly inward shifted configuration, in which the energetic particle confinement becomes nearly optimum in the LHD configurations. The triton burn-up simulation is also performed by GNET code, and we obtain a similar increase of the triton burn-up ratio depending on the magnetic configurations in LHD.

Introduction

The deuterium plasma experiment has been started from 2017 campaign in the Large Helical Device (LHD)[1]. The study of the energetic particle is one of the important issues in the deuterium plasma experiment of LHD. The nuclear fusion between deuterium ions produces the 2.5MeV neutron or 1MeV triton almost equal probability. Also, the produced 1MeV tritons react with the deuterium and produce 14MeV neutrons. The D-T fusion cross section has a peak at the energy of about 150keV and, then, the 1MeV tritons would react mostly after slow down to that energy. Therefore, the confinement of 1MeV tritons can be seen by measuring the produced neutrons[2].

Because of the three-dimensional magnetic configuration, the behaviors of trapped particles are complex, and the confinement of the energetic particle is an important issue in the heliotrons. The LHD has flexibility in the magnetic configuration controlling the poloidal magnetic field, etc. It is pointed out that the inward shift of the magnetic axis position in major radius, R_{ax} , improves the confinement of the energetic particles[3]. We have to confirm this fact experimentally to design the future fusion reactor in heliotron configurations. The confinement of energetic particle has been investigated in a hydrogen operation phase of LHD. The charge-exchange neutral particle analyzer (NPA) and scintillator-based fast-ion loss detector (FILD) have played a primary role in the measurement of energetic particles[4]. However, we can obtain an only limited physics information from these diagnostics. NPA can detect energetic particles having a limited pitch-angle along the line of sight and strongly depends on the density profile of neutral particles. We need information of the energetic particle in the important core region of plasma.

Triton burn-up experiment

Time-resolved 14 MeV neutron flux is measured by scintillating-fiber detectors. More than 20MW of NBI heating power is injected into deuterium plasma, and we obtain the electron and ion temperatures more than 3keV with the plasma density about $3 \times 10^{19} \text{m}^{-3}$. Figure 1 shows the typical time evolutions of total and 14MeV neutron rates. We can see that a build-up rate of 14 MeV neutron flux is slower than that of total neutron rate. It comes from cross-section curve for D-T reaction and the peak of the triton fusion reaction starts after the energy slow down about 150keV.

Triton burn-up ratio is evaluated in stellarator/heliotron devices for the first time. It is defined as a ratio of secondary DT neutron yield to total neutron yield. The scintillating-fiber detector is calibrated by using results measured with calibrated NAS. Therefore, triton burn-up ratio can be evaluated in every discharge in LHD.

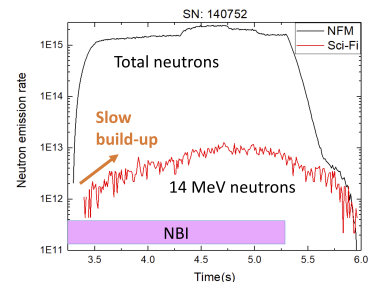


Figure 1: Typical time evolutions of total and 14MeV neutron rates.

Confinement property of helically trapped energetic ions largely depends on magnetic field configurations. The triton burn-up ratios are plotted as a function of R_{ax} (3.55m, 3.6m, 3.75m, and 3.9m) in Figure 2. A significant increase of triton burn-up ratio can be seen in the strongly inward shifted configuration. It is pointed out that the inward shift of the magnetic axis position in major radius, R_{ax} , improves the confinement of the energetic particles[3]. Figure 3 shows the typical orbit of trapped particle in the $R_{ax}=3.75\text{m}$ (left) and 3.55m (right) configurations. We can see a nearly optimum of confinement of the trapped particle in the $R_{ax}=3.55\text{m}$ configuration, where the large burn-up ratio is obtained.

Simulation analysis

We perform the triton burn-up simulation of the deuterium experiment of LHD and evaluate the D-T fusion reaction rates to compare with the experimental results of the 14 MeV neutron diagnostic system. The radial profile of the 1 MeV triton production rate due to the D-D fusion reaction between D-beam and D-thermal ions is evaluated by GNET. As a result, we obtain a center-peaked triton production rate.

Next, we solve the 5-D drift kinetic equation for the 1MeV tritons by GNET and evaluate the slow down distribution in the real and velocity space. Figure 4 shows the slowing down velocity space distribution of the 1MeV tritons in LHD ($R_{ax} = 3.6\text{m}$). We can see a relatively large loss region near the boundary of the passing and the helically trapped particles. About 25% of tritons escape with almost the initial energy of 1 MeV by the prompt orbit loss due to drift motion immediately after their birth ($t < 10^{-5}$ s). After the prompt orbit loss, the collisionless diffusive loss ($10^{-5} < t < 10^{-2}$) and, then, the collisional diffusive loss ($t > 10^{-2}$ s) become dominant.

It is found that the confinement of the 1MeV tritons is improved by the strongly inward shifted configuration of LHD ($R_{ax} = 3.5\text{m}$) and that the triton burn-up ratio is increased to about 0.1% (Fig. 2). This tendency agree with the experimental results and it well agrees also quantitatively if we add a constant factor 0.14% as an additional effect.

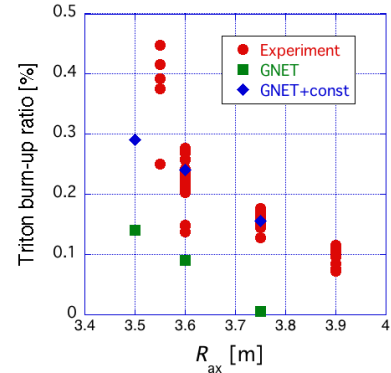


Figure 2: Triton Burn-up ratio as a function of R_{ax} (3.55m, 3.6m, 3.75m, and 3.9m).

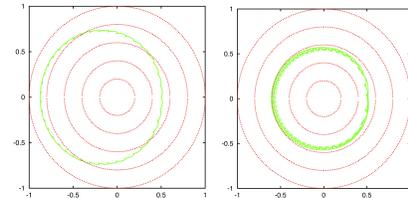


Figure 3: Typical orbit of trapped particle in the $R_{ax}=3.75\text{m}$ (left) and 3.55m (right) configurations.

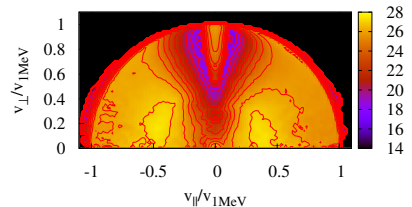


Figure 4: Slowing down velocity space distribution of the 1MeV tritons in LHD ($R_{ax} = 3.6\text{m}$).

- [1] M. Osakabe, et al., Fusion Sci. Technl. **71**, 199 (2017).
- [2] M. Isobe, et al., Rev. Sci. Instrum. 81 (2010) 10D310.
- [3] S. Murakami et al., Nuclear Fusion **42**, Nuclear Fusion 42 (2002) L19.
- [4] M. Isobe et al., Fusion Science and Technology 58, 426-435, 2010.
- [5] K. Ogawa et al., Nuclear Fusion 53, 053012, 2013.
- [6] S. Murakami et al., Nuclear Fusion **46**, S425 (2006).
- [7] H. Yamaguchi and S. Murakami, Nucl. Fusion **56** (2016) 026003.

Integrated transport simulation of LHD plasma by TASK3D

S. Maeta, S. Murakami, H. Yamaguchi, A. Fukuyama, K. Nagaoka^a, H. Takahashi^a,
H. Nakano^a, M. Osakabe^a, K. Tanaka^a, M. Yokoyama^a, and LHD Exp Group^a

Department of Nuclear Engineering, Kyoto University, Kyoto 615-8540, Japan

^aNational Institute for Fusion Science, 322-6 Oroshi-cho, Toki 509-5292, Japan

introduction

Various physical phenomena with wide ranges of time and space scales are connected in the fusion plasma. Thus, in order to predict the performance of the fusion plasma, an integrated simulation combining various physics models is required. Many integrated simulation code has been developed for tokamak and helical plasmas. TASK3D is an integrated simulation code for helical plasma and has been applied to the analyses of the plasma transport of LHD plasmas[1, 2].

The D-plasma experiment has been started from March 2017 in LHD, where the deuterium NBI heating beams with the power more than 30MW is injected to the deuterium plasma. Main objects of this project are to improve plasma performance, to make clear the isotope effect on the energy confinement and/or turbulent transport in high T_i plasma and to understand energetic ion confinement by D-D nuclear fusion neutron measurements.

In this paper, we verify the turbulent transport model of deuterium plasma in LHD using TASK3D. We evaluate the NBI heat deposition of deuterium plasma by GNET code[4, 5]. An integrated simulation of deuterium plasma has been performed assuming a transport model including transport improvement obtained in the H/He plasma simulation. In addition, we investigate the ECH plasma of LHD applying TASK3D and compare with the experimental results. We perform the integrated transport simulation by assuming several turbulent transport models.

Heat transport simulation of deuterium plasma and ECH plasma

In previous studies, hydrogen experiments are well reproduced by assuming gyro-Bohm(gB) for electron and gB+gradT for ion turbulence transport coefficients in hydrogen experiments[2] and H/He experiment results are well reproduced assuming A_{eff} depending model

$$\chi_i^{TB} = \overline{\chi_i^{TB}} \times \exp(-kF(A_{eff} - c)) \quad (1)$$

where $c = 1.4$, $k = 2.0$ and $F(x)$ is step function. We have selected hydrogen and deuterium plasma with similar density profiles (Fig.1). We compare the temperature profiles of experiment and simulation results to clarify the isotope effect on the turbulent

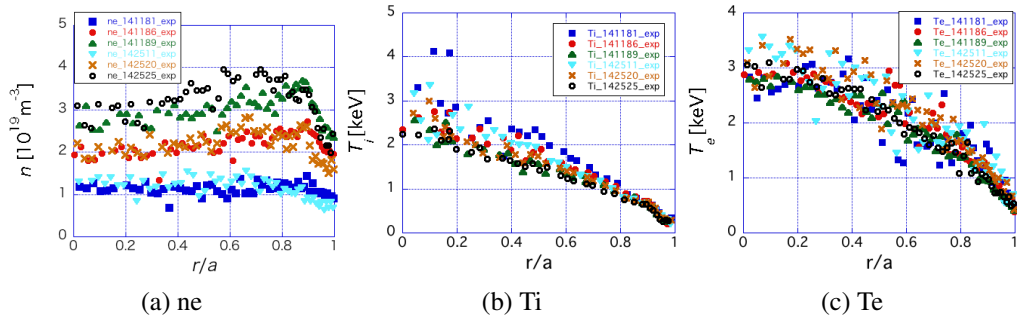


Figure 1: Experimental result of deuterium or hydrogen plasma.

transport. We investigate the heat transport of hydrogen and deuterium plasma using TASK3D and GNET.

First, we performed hydrogen plasma simulation assuming gB+gradT for ion and gB for electron turbulence transport model. We determine the coefficient of gB+gradT model so that the simulation result agree well with experimental results of hydrogen plasmas. Simulation result of hydrogen plasma (Fig.2) shows similar radial profile of T_i values.

Next, we performe the deuterium plasma simulation. We apply the gB+gradT model and A_{eff} depending models to the deuterium plasma assuming the coefficient of these model same as that of hydrogen plasma. Fig.3, 4 and 5 show simulation results of deuterum plasma. Simulation results with A_{eff} depending model agree well with the experimental results of T_i profiles in all three density cases.

Summary

We have developed the integrated simulation code TASK3D to predict the plasma performance in the 3D magnetic configuration plasma. We have investigated deuterium experimental plasma by the integrated simulation code TASK3D. We determine the coefficient of gB+gradT model so that the simulation result agree well with experimental results of hydrogen plasmas. Simulation results assuming the present turbulent transport model based on the H/He plasma good agree with the deuterium experimental results.

References

- [1] S. Murakami, et al., Plasma Phys. Control. Fusion **57** (2015) 054009.
- [2] A. Sakai, et al., Plasma Fusion Res. **9** (2014) 3403124.
- [3] K. Nagaoka, et al., Plasma Fusion Res. **11** (2016) 2402106

[4] H. Yamaguchi and S. Murakami, Plasma Fusion Res. **9** (2014) 3403127.

[5] S. Murakami, et al., Nuclear Fusion **46** (2006) S425.

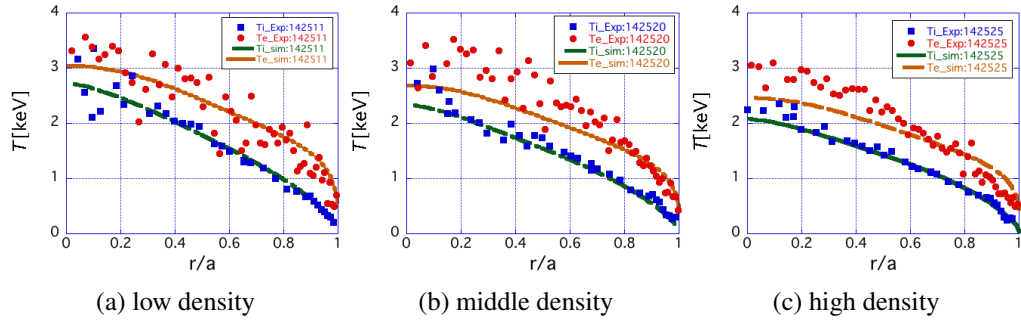


Figure 2: Simulation result of hydrogen plasma.

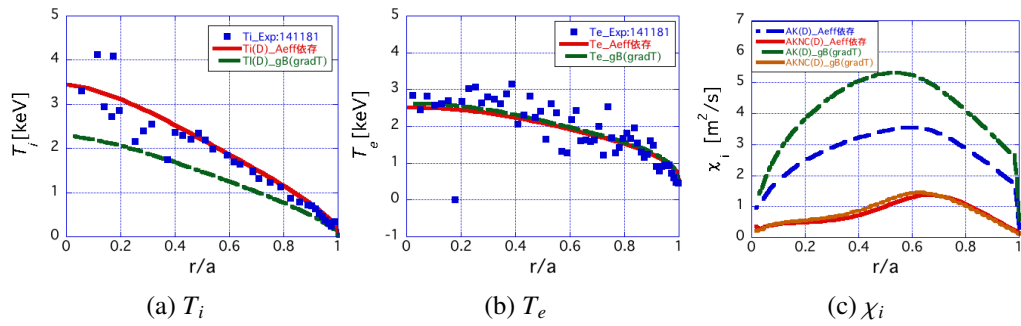


Figure 3: Simulation result of deuterium plasma of low density.

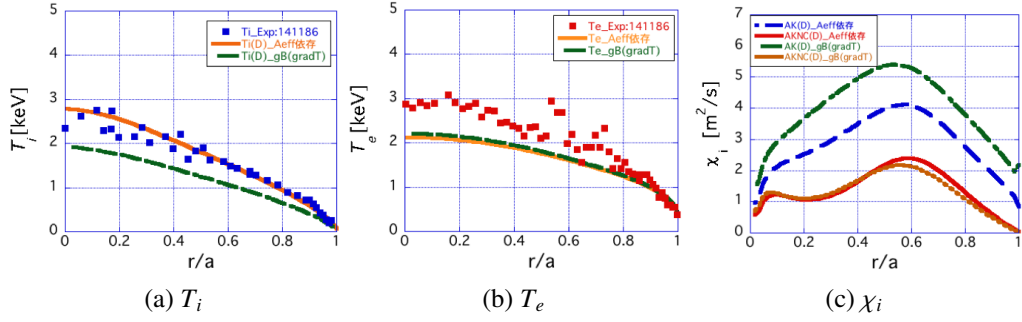


Figure 4: Simulation result of deuterium plasma of middle density.

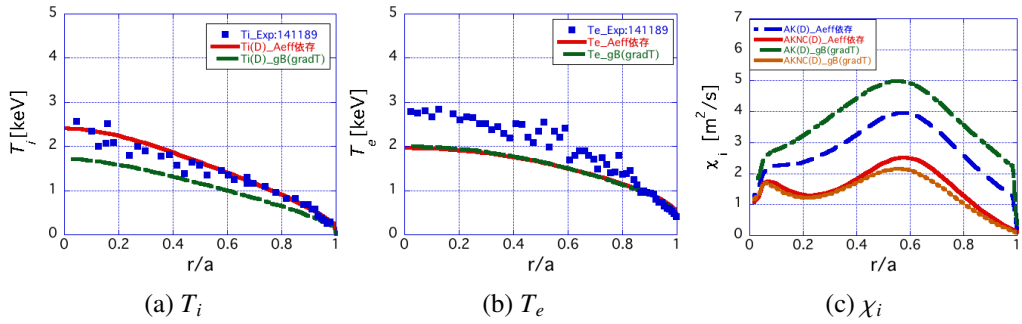


Figure 5: Simulation result of deuterium plasma of high density.

Effects of electron cyclotron heating on the toroidal flow in helical plasmas

Y.Yamamoto, S.Murakami, H.Yamaguchi¹, Chang Ching-Chieh, H.Takahashi¹

Graduate School of Engineering, Kyoto University

¹*National Institute of Fusion Science, Toki 509-9252, Japan*

Abstract

We study the behaviors of supra-thermal electrons by the electron cyclotron heating, which can generate the $j \times B$ torque and the collisional torque in the toroidal direction in the LHD plasma. We apply the GNET code, which can solve a linearized drift kinetic equation in 5-D phase space. As a result, we find that the obtained torque by ECH in the toroidal direction is comparable to that by NBI (neutral beam injection) and that its direction is opposite to NBI torque in the inner region.

1 Introduction

Recently, spontaneous toroidal flows in the ECH plasma have been observed in many tokamaks and helical devices e.g. JT-60U, HSX, and LHD. Many studies have been done experimentally[1] and theoretically[2]. Particularly, in LHD, when ECH was applied into the NBI heated plasma, the radial profile of the toroidal flow velocity changes drastically and the direction is reversed in the core region as shown in figure 1. This change of the toroidal flow by ECH has not yet been understood well.

In the previous studies, we have found that ECH generates a radial flux of energetic electrons in non-axisymmetric plasmas[3]. Therefore, the radial bulk ion current must flow to cancel this energetic electron current, and the bulk ion current could generate the toroidal torque by the $j \times B$ force. In this study, we investigate the behaviors of energetic electrons by ECH, which can generate the radial current making the $j \times B$ torque in the LHD plasma. Also, we evaluate the collisional torques, by the collision between energetic electrons and bulk plasma. We apply the GNET code, which can solve a linearized drift kinetic equation for energetic electrons by ECH in 5-D phase space[3]. Then, we calculate the toroidal flow by solving the radial diffusion equation including the toroidal component of the $j \times B$ torque, collisional torques, and the NBI torque, which is evaluated by FIT-3D code[4].

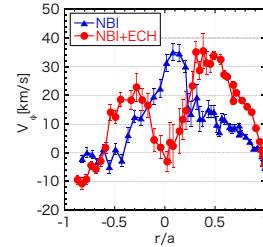
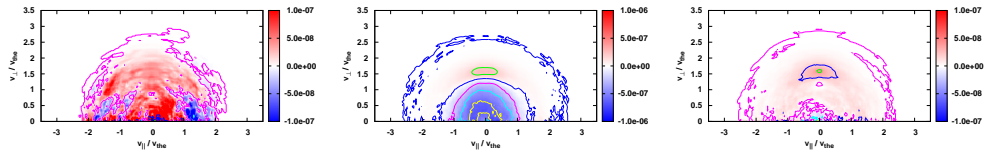


Figure 1: The toroidal flow change in the LHD experiment.

2 Simulation model

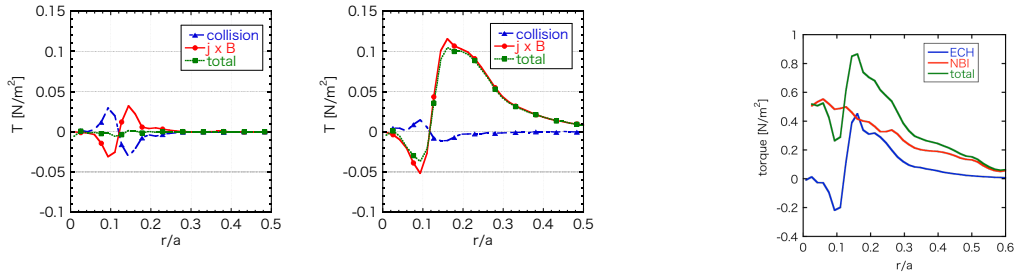
In order to study ECH, we apply the GNET code, which can solve a linearized drift kinetic equation for energetic electrons in 5-D phase space. We can write the gyrophase averaged electron distribution function as

$$f(\mathbf{r}, v_{\parallel}, v_{\perp}) = f_{\text{Max}}(r, v^2) + \delta f(\mathbf{r}, v_{\parallel}, v_{\perp}) \quad (1)$$



(a) $r/a \sim 0.00$:The inner re- (b) $r/a \sim 0.15$:The region of (c) $r/a \sim 0.25$:The outer re-
 gion of the deposition. the deposition. gion of the deposition.

Figure 2: The velocity distribution of δf



(a) Axisymmetry

(b) LHD

Figure 4: NBI and ECH

Figure 3: The $j \times B$ and collisional torques by ECH(1MW). torques.

where f_{Max} represents Maxwellian, and \mathbf{r} , v_{\parallel} and v_{\perp} are the particle position vector, the parallel and perpendicular velocity, respectively. The drift kinetic equation for δf is given by

$$\frac{\partial \delta f}{\partial t} + (\mathbf{v}_d + \mathbf{v}_{\parallel}) \cdot \frac{\partial \delta f}{\partial \mathbf{r}} + \dot{v} \cdot \frac{\partial \delta f}{\partial \mathbf{v}} - C(\delta f) - L(\delta f) = S^{\text{ql}}(f_{\text{Max}}) \quad (2)$$

where \mathbf{v}_d is the drift velocity. $C(\delta f)$, $L(\delta f)$ and $S^{\text{ql}}(\delta f)$ are linear collision operator, orbit loss, and the quasi-linear diffusion operator for the absorption of ECH, respectively.

3 Results

Figure 2 shows the velocity distribution of δf at each minor radius. We can see that more energetic electrons can be found outer / inner regions apart from the heating point($r/a \sim 0.15$). Thus, the radial electron flux is produced and it makes ion return current.

The $j \times B$ and collisional torques cancel each other in axisymmetric plasma[5]. We first calculate the torques in the axisymmetric magnetic configuration. As shown in figure 3(a), we obtain this cancellation of the toroidal torques. Next, we study the behaviors of energetic electrons and evaluate the torques assuming the LHD plasma. Figure 3(b) shows that the $j \times B$ torque is larger than the collisional torque sufficiently in LHD. Figure 4 shows the torques with experimental heating parameters. As a result, we find that the obtained torque by ECH is almost same order as NBI torque and that its direction is opposite to NBI torque in the inner region.

We evaluate the toroidal flow velocity V_{ϕ} solving the radial diffusion equation

$$\frac{\partial V_{\phi}}{\partial t} = \frac{1}{r} \frac{\partial}{\partial r} \left(r D \frac{\partial V_{\phi}}{\partial r} \right) + \frac{1}{m_i n_i R} (T_{\text{ECH}} + T_{\text{NBI}} + T_{\text{NTV}}) \quad (3)$$

where T and D are torques by ECH, NBI or Neoclassical Toroidal Viscosity (NTV) and radial diffusivity of toroidal flow. T_{NTV} is given as

$$T_{\text{NTV}} = -m_i n_i \mu_{\text{ti}} \frac{\delta B^2}{B_0^2} \langle R V_\phi \rangle \quad (4)$$

where μ_{ti} is the viscosity coefficient and we set its value as the order of 10^5 . In the calculation, we assume that ECH is superposed into the NBI plasma. Figure 5 shows the change of toroidal flows by ECH. The $j \times B$ torque of ECH makes the toroidal flow reduce / enhance at the inner/outer of heating point. It agrees with the experiment observations qualitatively.

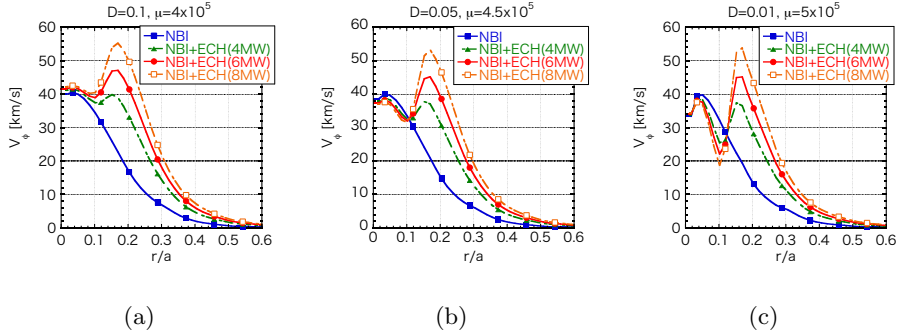


Figure 5: Change of toroidal flows by ECH

4 Conclusion

We have evaluated the behaviors of energetic electrons by ECH applying GNET code in order to make clear the mechanism of the toroidal flow change in LHD plasma heated by ECH and NBI. The obtained $j \times B$ torque is the same order as NBI torque and its direction agree with experiment observation.

References

- [1] M.Yoshida, *et al.*, Nucl. Fusion **49** 115028 (2009)
- [2] P. H. Diamond, *et al.*, Nucl. Fusion **53** 104019 (2013)
- [3] S. Murakami, *et al.*, Nucl. Fusion **40** 693 (2000)
- [4] S. Murakami, *et al.*, Fusion Technol. **27** 256 (1995)
- [5] M. N. Rosenbluth and F. L. Hinton, Nucl. Fusion **36** 55 (1996)

PARASOL Simulation of ELM Heat Flux in Tokamak SOL-Divertor Plasma

T. Takizuka¹, M. Hosokawa², A. Loarte², N. Hayashi³

¹ Graduate School of Engineering, Osaka University, Suita 565-0871, Japan

² ITER Organisation, Route de Vinon sur Verdon, CS 90 046, 13067 St Paul Lez Durance Cedex, France

³ National Institutes for Quantum and Radiological Science and Technology, Naka 311-0193, Japan

Two-dimensional PARASOL simulations on the ELM heat flux in SOL-divertor plasmas of a realistic small tokamak are carried out. The in/out divertor asymmetry of the ELM deposition energies, E_{ELM}^{inner} and E_{ELM}^{outer} , is studied. Results, i.e., $E_{ELM}^{inner} \gtrsim E_{ELM}^{outer}$ for the ion ∇B drift towards an X-point, while $E_{ELM}^{outer} > E_{ELM}^{inner}$ for the ion ∇B drift opposite to an X-point, agree well with the experimental observations.

1. Introduction

Edge localized modes (ELMs) are of the most concern for the erosion of divertor plates in ITER [1]. An uncontrolled type-I ELM in ITER Q = 10 operation is predicted to release a very large loss energy of $\Delta W_{ELM} \sim 20$ MJ [2]. This exceeds much the melting condition of ITER tungsten divertor plate. When a characteristic time duration of an ELM heat deposition on the divertor plate is assumed $\tau_{dep} \sim 2\tau_{||} \sim 0.2-0.5$ ms ($\tau_{||} = \pi qR/C_s$ [3]) for $q \sim 4$, $R \sim 6$ m, and $C_s \sim 4 \times 10^5$ m/s at $T > 1$ keV, the acceptable energy density is estimated as $Q_{ELM} = 0.5$ MJ/m² and the allowed upper limit of ELM energy loss is $\Delta W_{ELM}^{lim} = 0.7$ MJ [4]. Here the wetted area for ELMs in ITER is expected as $A_{ELM} = 4\pi R \lambda_{ELM} g_{div} \sim 1.5$ m² with a mid-plane ELM-heat-flux width of $\lambda_{ELM} \sim 2$ mm and a geometric expansion factor $g_{div} \sim 10$. Thus the ELM control methods to reduce ΔW_{ELM} are required in ITER [5].

When the in/out divertor asymmetry is taken into account, the allowed upper limit ΔW_{ELM}^{lim} becomes small. The above estimation is based on the empirical extrapolations from limited number of experimental data. In order to assure the prediction for ITER, theoretical understanding of ELM behaviors is indispensable. MHD simulations have been carried out for this sake. JOEUK simulations, for example, showed that the ELM-heat-deposition duration Δt was shorter than an expected sound-speed flight time $\tau_{||}$, and that the ELM deposition energy E_{ELM} was always larger on the outer divertor plate than on the inner, $E_{ELM}^{outer} > E_{ELM}^{inner}$ [6]. The in/out asymmetry of E_{ELM} observed in tokamak experiments, however, is varied by the ∇B direction; $E_{ELM}^{inner} > E_{ELM}^{outer}$ for the ion ∇B drift towards an X-point (normal direction), while $E_{ELM}^{outer} > E_{ELM}^{inner}$ for the ion ∇B drift opposite to an X-point (reversed direction) [7].

Kinetic effects are considered very important for the transport physics in edge plasmas [8,9]. Since the MHD modeling does not include the kinetic effect, kinetic particle simulations have been carried out to study the transient ELM-loss behaviors in SOL-divertor plasmas, at first in one-dimension (1D) systems [10-14]. Recently we have extended these simulations to ITER scale with 1D PARASOL code [15,16]. Although valuable findings on the ELM-loss dynamics in SOL-divertor plasmas, e.g., $\tau_{dep} \sim \tau_{||}$ in contrast to the JOEUK result, were obtained from 1D kinetic particle simulations, the in/out divertor asymmetry dependent on the ∇B direction was not realized by the 1D PARASOL of course. Two-dimensional (2D) kinetic simulations are required to solve this problem. The PARASOL simulations for 2D tokamak systems demonstrated a drastic change of the stationary SOL flow pattern by the ∇B direction [17]. The in/out asymmetry in the stationary SOL flow is mainly caused by the "ion-orbit-induced flow" [18]. For the in/out divertor asymmetry of transient ELM heat flux, the kinetic effect can play an important role, too. In this proceedings paper, we present 2D PARASOL simulations on the ELM heat flux in SOL-divertor plasmas of a realistic small tokamak, and show the

in/out divertor asymmetry of the ELM deposition energies, E_{ELM}^{inner} and E_{ELM}^{outer} , which is dependent on the ∇B direction.

2. 2D PARASOL simulation for transient ELM event

2D PARASOL code has been developed to simulate an axisymmetric tokamak plasma surrounded by SOL-divertor plasmas including the sheath in front of divertor plates [9,17,19]. Gyration orbits of ions are fully traced, while guiding-center orbits are followed for electrons. It is essential to trace the full ion motion for the correct drift movement including the exact polarization drift. The electrostatic field is calculated consistently coupled with equations of motion for all charged particles. Effects of Coulomb collisions are added by applying a binary collision model so called Takizuka-Abe model [20]. The anomalous transport is simulated with a Monte-Carlo random-walk model. A spatial displacement perpendicular to \mathbf{B} , Δ_{\perp} , is added for every time step Δt both on electrons and ions. The isotropic displacement is given by a Gaussian random number with $\langle \Delta_{\perp} \rangle = 0$ and $\langle \Delta_{\perp}^2 \rangle = D_{anom} \Delta t$ ($\langle \rangle$: ensemble average, D_{anom} : anomalous diffusion coefficient). Hot source particles are supplied in the central core region, and cold recycled particles are supplied near the divertor plate.

In order to simulate a transient ELM event, an ELM modeling of the diffusion type is implemented in 2D PARASOL code [16,21]. After a quasi-stationary plasma (as an inter-ELM phase) is obtained, a large diffusion coefficient D_{ELM} is suddenly put in a selected region near the outer mid-plane (see Fig. 1) during a short duration τ_{ELM} . Particles in this core peripheral region are expelled to the SOL region and flow out to the in/out divertor plates along \mathbf{B} . It was found in Refs. [16] and [21] that the ∇B -direction dependence of in/out divertor asymmetry in E_{ELM} was the same as that for experimental observations. In these 2D PARASOL simulations, plasma parameters were given as normalized ones, i.e., normalized ion Larmor radius $\rho_{i*} = \rho_i/a \sim 1/50$ and wide range of normalized collisionality $\nu_* = L_{\parallel}/l_{mfp}$ (L_{\parallel} : connection length, l_{mfp} : mean free path). The cross-sectional plasma shape was set very simple.

For the sake of direct comparison between PARASOL 2D results and experimental ones, we adopt the real scale plasma parameters and a realistic plasma shape. The parameters are of a typical COMPASS plasma [22]; major radius $R = 0.56$ m, minor radius $a = 0.2$ m, elongation $\kappa = 1.87$, magnetic field $B_t = 1.2$ T, plasma current $I_p = 340$ kA, and the cross-sectional plasma shape as shown in Fig. 1 [23]. The electron density in the core peripheral region is about $n_e \approx 3 \times 10^{19}/\text{m}^3$ and temperatures are about $T_e \approx T_i \approx 70$ eV, which correspond to the normalized values of $\rho_{i*} \approx 1/150$ for D^+ ion and $\nu_* \approx 10$ for $Z_{eff} = 2.5$. Stationary D_{anom} is set $1 \text{ m}^2/\text{s}$ for an example. The value of D_{ELM} during $\tau_{ELM} = 200 \mu\text{s}$ and its enhanced region are chosen properly so that the total ELM loss energy becomes a planned value $\Delta W_{ELM} \sim 80\text{-}270$ J, which is 10-30 % of the so-called pedestal confined energy W_{ped} .

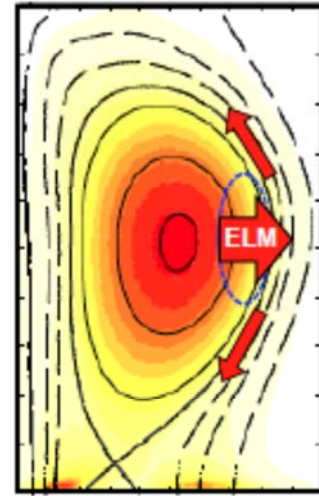


Fig. 1 COMPASS-like plasma shape in a rectangular wall. Hot particles in the core peripheral region near outer mid-plane are expelled to the SOL region by ELM, and flow out to in/out divertor plates along \mathbf{B} .

3. In/out divertor asymmetry in the ELM heat flux and deposition energy [23]

Simulation results are shown in Fig. 2, where particle recycling rate at the divertor plate is set $R_{recy} = 0.3$ and the total ELM loss energy is $\Delta W_{ELM} \sim 100$ J. Profiles of ELM heat flux q on the divertor plate at a time $75 \mu\text{s}$ after ELM event start are compared between cases of (a) normal and (b) reversed ∇B

directions. It is clearly found that the in/out divertor asymmetry in the ELM heat flux is owed by the strong dependence of ion heat flux component on the ∇B direction. Time traces of heat flux peaks q_{peak} of ion and electron components on the inner (open circles) and outer (closed circles) divertors are shown in Fig. 3 for (a) normal and (b) reversed cases. Electron heat flux reaches at first ($\sim 1 \mu s$) the outer plate (near the ELM loss region) and next ($\sim 5 \mu s$) the inner plate. Ion heat flux reaches the plates with the time scale of $\tau_{ij} = 10\text{-}20 \mu s$, and interestingly increases much in the second stage after $t = 40 \mu s$. In this second stage, the in/out divertor asymmetry in the ion heat flux component becomes remarkable; $q_{peak}^{inner} > q_{peak}^{outer}$ for normal case while $q_{peak}^{outer} > q_{peak}^{inner}$ for reversed case. The physical mechanism of this dependency will be studied in detail by our future work.

The in/out divertor asymmetry in the ELM deposition energy $E_{ELM} = \int dt \int 2\pi R q dR$ is summarized in Fig. 4 for various conditions; low recycling ($R_{recy} = 0.3$) / high recycling ($R_{recy} = 0.9$) and small ELM ($\Delta W_{ELM} \sim 100 \text{ J}$) / large ELM ($\Delta W_{ELM} \sim 300 \text{ J}$). For the reversed case (red symbols), the asymmetry of $E_{ELM}^{outer} > E_{ELM}^{inner}$ is robust. On the other hand for the normal case (blue symbols), the asymmetry is not simply the same aspect of $E_{ELM}^{inner} > E_{ELM}^{outer}$ as $q_{peak}^{inner} > q_{peak}^{outer}$ seen in Fig. 3 (a). The asymmetry, $E_{ELM}^{inner} \gtrsim E_{ELM}^{outer}$ becomes small or rather opposite when the recycling is large. Thermoelectric current from outer divertor to inner divertor, which brings ELM electron heat from inner to outer, becomes large with the increase of recycling. Thus the asymmetry is compensated by this electron heat channel especially for the normal case. The reason why this compensation is unremarkable for the reversed case will be studied in future.

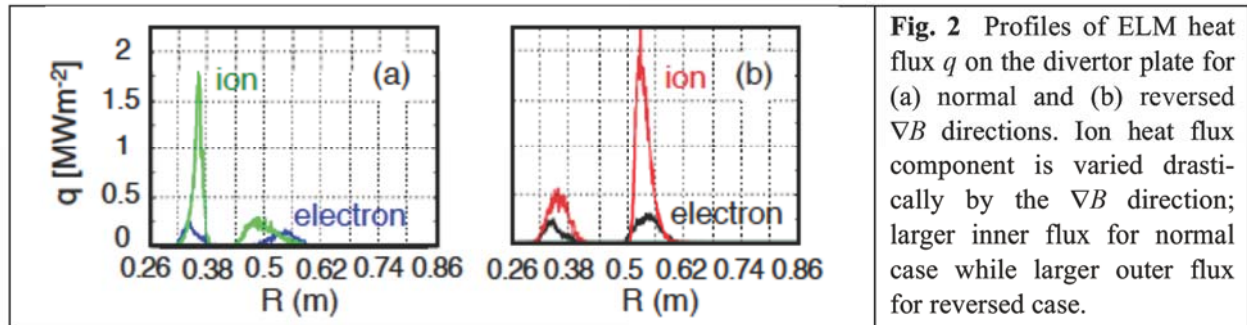


Fig. 2 Profiles of ELM heat flux q on the divertor plate for (a) normal and (b) reversed ∇B directions. Ion heat flux component is varied drastically by the ∇B direction; larger inner flux for normal case while larger outer flux for reversed case.

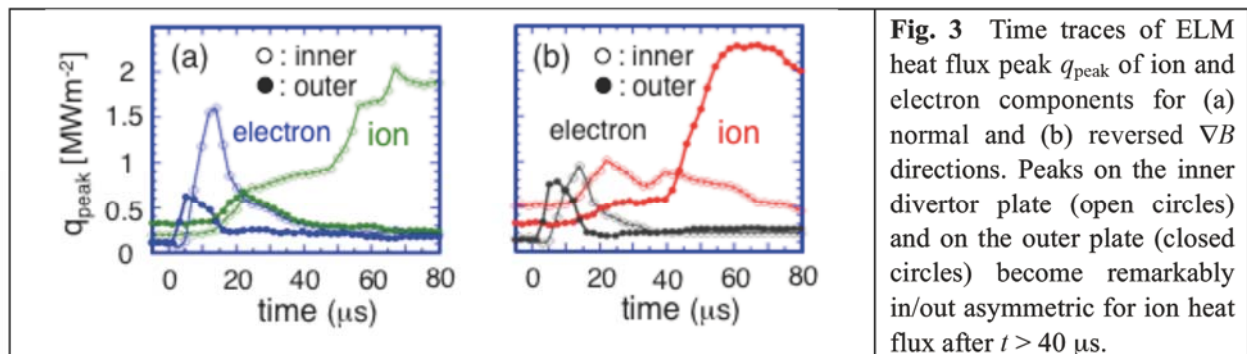


Fig. 3 Time traces of ELM heat flux peak q_{peak} of ion and electron components for (a) normal and (b) reversed ∇B directions. Peaks on the inner divertor plate (open circles) and on the outer plate (closed circles) become remarkably in/out asymmetric for ion heat flux after $t > 40 \mu s$.

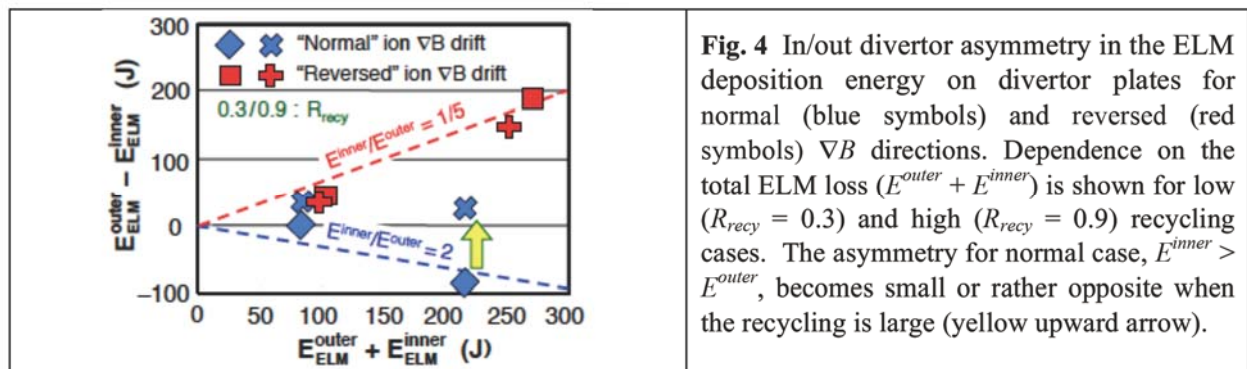


Fig. 4 In/out divertor asymmetry in the ELM deposition energy on divertor plates for normal (blue symbols) and reversed (red symbols) ∇B directions. Dependence on the total ELM loss ($E^{outer} + E^{inner}$) is shown for low ($R_{recy} = 0.3$) and high ($R_{recy} = 0.9$) recycling cases. The asymmetry for normal case, $E^{inner} > E^{outer}$, becomes small or rather opposite when the recycling is large (yellow upward arrow).

4. Summary and discussion

Effect of ∇B direction on the in/out divertor asymmetry in ELM heat load is studied using PARASOL 2D code for a COMPASS-scale tokamak. Direction of ion ∇B drift has a strong influence on the in/out divertor asymmetry. ELM ion heat flux flows mainly to inner divertor for the normal ion ∇B drift, while to outer divertor for the reversed ion ∇B drift. Asymmetry in the ELM deposition energy of $E_{ELM}^{outer} > E_{ELM}^{inner}$ for the reversed case is robust. On the other hand, asymmetry for the normal case ($E_{ELM}^{inner} \gtrsim E_{ELM}^{outer}$) is compensated by the electron heat channel due to thermoelectric current from outer divertor to inner divertor, which becomes large with the increase of recycling. These simulation results are in good qualitative agreement with experiments, although magnitude of predicted changes is a bit larger than that of typical experimental measurements.

Further 2D PARASOL simulations closer to COMPASS parameters are in progress to refine these findings by comparing with experiments. Physical mechanisms of the in/out divertor asymmetry in ELM heat flux and heat load will be investigated in detail by our future work. The results will be published by MH et al. in the near future.

Acknowledgements We thank Drs. G.T.A. Huijsmans, J. Adamek and J. Seidl for the ongoing collaboration on ELM simulations for ITER. One of the authors, TT, is grateful to Prof. Y. Ueda, Dr. K. Imano and Prof. Y. Ogawa for their supports and encouragements.

References

- [1] G. Federici et al., Plasma Phys. Control. Fusion **45** (2003) 1523.
- [2] A. Loarte et al., Plasma Phys. Control. Fusion **45** (2003) 1549.
- [3] A. Loarte et al., J. Nucl. Mater. **313-316** (2003) 962.
- [4] A. Loarte et al., Proc. 23rd Int. Conf. on Fusion Energy (Daejeon, South Korea, 2010) ITR/1-4, www.naweb.iaea.org/naweb/physics/FEC/FEC2010/index.htm.
- [5] A. Loarte et al., Nucl. Fusion **54** (2014) 033007.
- [6] G.T.A. Huijsmans, A. Loarte, Nucl. Fusion **53** (2013) 123023.
- [7] T. Eich et al., J. Nucl. Mater. **363-365** (2007) 989.
- [8] R. Cohen, X.Q. Xu, Contrib. Plasma Phys. **48** (2008) 212.
- [9] T. Takizuka, Plasma Phys. Control. Fusion **59** (2017) 034008.
- [10] A. Bergmann, Nucl. Fusion **42** (2002) 1162.
- [11] T. Takizuka, M. Hosokawa, Contrib. Plasma Phys. **46** (2006) 698.
- [12] T. Takizuka, M. Hosokawa, Trans. Fusion Sci. Technol. **51** (2007) 271.
- [13] T. Takizuka, N. Oyama, M. Hosokawa, Contrib. Plasma Phys. **48** (2008) 207.
- [14] D. Tskhakaya et al., J. Nucl. Mater. **390-391** (2009) 335.
- [15] M. Hosokawa, A. Loarte, G.T.A. Huijsmans, T. Takizuka, N. Hayashi, Proc. 41st EPS Conf., (Berlin, Germany, 2014) P5.003, <http://ocs.ciemat.es/EPS2014PAP/html>.
- [16] M. Hosokawa, A. Loarte, G.T.A. Huijsmans, T. Takizuka, N. Hayashi, Plasma Fusion Res. **11** (2016) 1403104.
- [17] T. Takizuka, K. Shimizu, N. Hayashi, M. Hosokawa, M. Yagi, Nucl. Fusion **49** (2009) 075038.
- [18] T. Takizuka, K. Hoshino, K. Shimizu, M. Yagi, Contrib. Plasma Phys. **50** (2010) 267.
- [19] T. Takizuka, Plasma Sci. Technol. **13** (2011) 316.
- [20] T. Takizuka, H. Abe, J. Comput. Phys. **25** (1977) 205.
- [21] M. Hosokawa, A. Loarte, G. Huijsmans, T. Takizuka, N. Hayashi, 43rd EPS Conf. on Plasma Physics (Leuven, Belgium, 2016) P4.073, <http://ocs.ciemat.es/EPS2016PAP/html>.
- [22] R. Panek et al., Plasma Phys. Control. Fusion **58** (2016) 014015.
- [23] M. Hosokawa, A. Loarte, G.T.A. Huijsmans, T. Takizuka, N. Hayashi, J. Adamek, J. Seidl, "Kinetic modelling of divertor fluxes between and during ELMs in a COMPASS-like tokamak plasma", 16th Int. Workshop on Plasma Edge Theory in Fusion Devices, (Marseille, France, 2017).

Effect of parallel viscosity approximation in inhomogeneous magnetic fields on SOL-divertor plasma profiles

Satoshi Togo, Tomonori Takizuka^{a)}, Mizuki Sakamoto, Naomichi Ezumi, Yuichi Ogawa^{b)}, Kenzo Ibano^{a)}, Kunpei Nojiri, Yue Li^{b)}, Yousuke Nakashima

Plasma Research Center, University of Tsukuba, 1-1-1 Tennodai, Tsukuba 305-8577, Japan

^{a)}Graduate school of Engineering, Osaka University, 2-1 Yamadaoka, Suita 565-0871, Japan

^{b)}Graduate School of Frontier Sciences, University of Tokyo, 5-1-5 Kashiwanoha, Kashiwa 277-8568, Japan

The effect of parallel viscous approximation on plasma profiles is studied on a one-dimensional scrape-off layer (SOL)-divertor system by comparing the profiles from two plasma fluid models; the Braginskii model and the anisotropic-ion-pressure (AIP) model. In a collisional plasma, profiles from two models agree fairly well while a clear deviation is obtained in a collisionless plasma. In the latter case, the viscous flux-limiting model was used beyond its criterion for physical validity which can be important in order to reproduce the behavior of detached plasmas with the Braginskii model.

1 Introduction

For designing divertors of future fusion devices, it is expected to develop a simulation code for plasmas in scrape-off layer (SOL) and divertor regions which considers all of important physical processes and is computationally realistic. Various SOL-divertor plasma code packages have been developed such as SOLPS (B2-EIRENE) [1], SONIC [2, 3] and UEDGE [4]. These code packages can basically reproduce experimental results fairly well. However, in some cases, especially detached plasmas, the agreement between experimental and numerical results is not satisfactory [5, 6].

Conventional code packages are based on a plasma fluid model derived by Braginskii [7] and the kinetic effect, which becomes essential in collisionless conditions, is considered by introducing some flux-limiting models to the heat and viscous fluxes [8]. For the parallel viscous flux, which is an approximation of the anisotropic part of the ion pressure, it is possible to exclude it (or make it automatically considered) by directly introducing the anisotropic ion pressure (AIP) to the plasma fluid model. In this paper, the effect of parallel viscous approximation on plasma profiles is studied by comparing the profiles from the Braginskii model and the AIP one on a one-dimensional SOL-divertor system.

2 Models

2.1 Anisotropic-ion-pressure (AIP) model

Basic plasma fluid equations of the AIP model are given as follows [9, 10];

$$\frac{\partial n}{\partial t} + B \frac{\partial}{\partial s} \left(\frac{nV}{B} \right) = S, \quad (1)$$

author's e-mail: togo@prc.tsukuba.ac.jp

$$\frac{\partial}{\partial t} (m_i n V) + B \frac{\partial}{\partial s} \left[\frac{1}{B} (m_i n V^2 + p_{i,\parallel} + p_e) \right] + \frac{p_{i,\perp} + p_e}{B} \frac{\partial B}{\partial s} = M_m, \quad (2)$$

$$\begin{aligned} & \frac{\partial}{\partial t} \left(\frac{1}{2} m_i n V^2 + \frac{1}{2} p_{i,\parallel} \right) \\ & + B \frac{\partial}{\partial s} \left[\frac{1}{B} \left(\frac{1}{2} m_i n V^3 + \frac{3}{2} p_{i,\parallel} V + q_{i,\parallel} \right) \right] \\ & + \frac{p_{i,\perp} V + q_{i,\perp}}{B} \frac{\partial B}{\partial s} \\ & = Q_{i,\parallel} + \frac{p_{i,\perp} - p_{i,\parallel}}{\tau_{\text{rx}}} + \frac{m_e}{m_i} \frac{p_e - p_{i,\parallel}}{\tau_e} - V \frac{\partial p_e}{\partial s}, \end{aligned} \quad (3)$$

$$\begin{aligned} & \frac{\partial p_{i,\perp}}{\partial t} + B \frac{\partial}{\partial s} \left(\frac{p_{i,\perp} V + q_{i,\perp}}{B} \right) - \frac{p_{i,\perp} V + q_{i,\perp}}{B} \frac{\partial B}{\partial s} \\ & = Q_{i,\perp} + \frac{p_{i,\parallel} - p_{i,\perp}}{\tau_{\text{rx}}} + \frac{2m_e}{m_i} \frac{p_e - p_{i,\perp}}{\tau_e}, \end{aligned} \quad (4)$$

$$\begin{aligned} & \frac{\partial}{\partial t} \left(\frac{3}{2} p_e \right) + B \frac{\partial}{\partial s} \left[\frac{1}{B} \left(\frac{5}{2} p_e V + q_e \right) \right] \\ & = Q_e + \frac{3m_e}{m_i} \frac{p_i - p_e}{\tau_e} + V \frac{\partial p_e}{\partial s}. \end{aligned} \quad (5)$$

Here, the pressure is defined by $p_\sigma = nT_\sigma$ in which $\sigma \in \{(i, \parallel), (i, \perp), i, e\}$. The effective-isotropic ion temperature is defined by $T_i \equiv (T_{i,\parallel} + 2T_{i,\perp})/3$. Other notations are the same as Ref. [11]. The ion-pressure relaxation time is given by $\tau_{\text{rx}} = 2.5\tau_i$ [12] in which the ion-ion Coulomb collision time τ_i is estimated by using T_i . The electron conductive heat flux q_e is estimated by a harmonic average of the Spitzer-Härm heat conduction $q_e^{\text{SH}} = -\kappa_e^{\text{SH}} (\partial T_e / \partial s)$ and a free-streaming heat flux $q_e^{\text{FS}} = nT_e \sqrt{T_e/m_e}$ as $q_e = [1/q_e^{\text{SH}} + 1/(\alpha_e q_e^{\text{FS}})]^{-1}$ in which the heat-flux limiting factor of electron is set to be $\alpha_e = 0.5$. The ion conductive heat fluxes, $q_{i,\parallel}$ and $q_{i,\perp}$, are estimated by the Spitzer-Härm heat conduction as $q_{i,\parallel}^{\text{SH}} = -(1/3)\kappa_i^{\text{SH}} (\partial T_{i,\parallel} / \partial s)$ and $q_{i,\perp}^{\text{SH}} = -(2/3)\kappa_i^{\text{SH}} (\partial T_{i,\perp} / \partial s)$, so that the total ion conductive heat

flux is $q_i = q_{i,\parallel}^{\text{SH}} + q_{i,\perp}^{\text{SH}} = -\kappa_i^{\text{SH}} (\partial T_i / \partial s)$. A virtual divertor model is used for the sheath boundary conditions [13, 14].

2.2 B2 code

The B2 code [15] is one of the most famous codes for the SOL-divertor plasma based on the Braginskii model. Although the B2 code is a two-dimensional code, it is applied to a one-dimensional system in this study by neglecting all of radial transports. By rewriting Eq. (2) in terms of the isotropic, $p_i \equiv (p_{i,\parallel} + 2p_{i,\perp})/3$, and anisotropic, $\delta p_i \equiv 2(p_{i,\parallel} - p_{i,\perp})/3$, parts of the ion pressure instead of $p_{i,\parallel}$ and $p_{i,\perp}$, the equivalent equation of parallel momentum of plasma in the Braginskii model is obtained as follows;

$$\begin{aligned} \frac{\partial}{\partial t} (m_i n V) + B \frac{\partial}{\partial s} \left(\frac{m_i n V^2}{B} \right) \\ + B^{3/2} \frac{\partial}{\partial s} (B^{-3/2} \delta p_i) = -\frac{\partial}{\partial s} (p_i + p_e) + M_m, \end{aligned} \quad (6)$$

in which δp_i is approximated by the following viscous flux;

$$\delta p_i \approx -\eta_i B^{-1/2} \frac{\partial}{\partial s} (B^{1/2} V) \equiv \pi_i. \quad (7)$$

Here, the following flux-limiting model is used in estimating the effective parallel-ion viscosity η_i ;

$$(1 + \Omega_\eta) \eta_i = \eta_{\text{cl}} \equiv 0.96 p_i \tau_i, \quad \Omega_\eta = \frac{\eta_{\text{cl}}}{\beta p_i} \left| \frac{\partial V}{\partial s} \right|. \quad (8)$$

In this study, the viscous-flux limiting factor is set to be $\beta = 4/7$ [8]. Note that η_i always becomes a finite positive value because Ω_η is positive or zero.

For the Bohm criterion at the sheath edge, $V \geq c_s$ is imposed in which V is extrapolated if it tends to be higher than the ion sound speed $c_s \equiv \sqrt{(T_i + T_e)/m_i}$.

By summing Eqs. (3) and (4), the equivalent equation of ion energy in the Braginskii model is obtained as follows;

$$\begin{aligned} \frac{\partial}{\partial t} \left(\frac{1}{2} m_i n V^2 + \frac{3}{2} p_i \right) \\ + B \frac{\partial}{\partial s} \left[\frac{1}{B} \left(\frac{1}{2} m_i n V^3 + \frac{5}{2} p_i V + \pi_i V + q_i \right) \right] \\ = Q_i + \frac{3m_e}{m_i} \frac{p_e - p_i}{\tau_e} - V \frac{\partial p_e}{\partial s}. \end{aligned} \quad (9)$$

Here, $Q_i = Q_{i,\parallel} + Q_{i,\perp}$ and the ion conductive heat flux q_i is estimated by the Spitzer-Härm heat conduction $q_i^{\text{SH}} = -\kappa_i^{\text{SH}} (\partial T_i / \partial s)$. Other equations are the same as those of the AIP model.

2.3 Calculation conditions

In this study, one-dimensional (parallel-to- \mathbf{B} direction the coordinate of which is denoted by s) plasmas in a SOL-divertor-like system are simulated by the B2 code

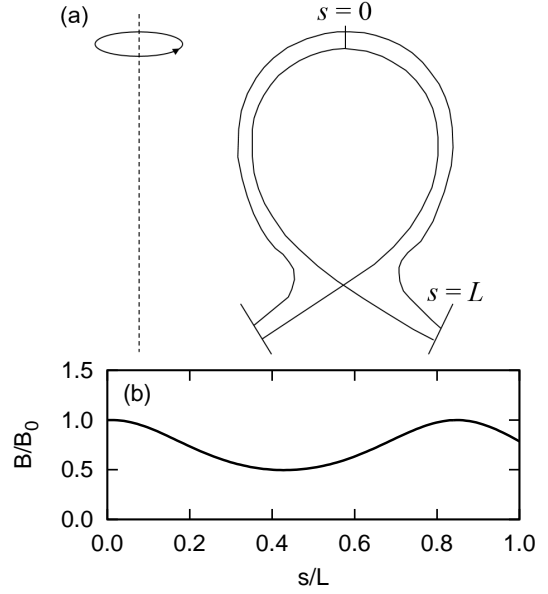


Fig. 1 (a) Schematic picture of a cross section of a tokamak and (b) normalized magnetic field B/B_0 as a function of the normalized parallel coordinate s/L .

and the AIP model. Figure 1 (a) shows a schematic picture of a poloidal cross section of a tokamak plasma. Plasmas in the outer (low-field side) SOL-divertor-like system are simulated roughly taking into account the dependence of the magnetic field strength on the major radius, $B \propto R^{-1}$. Figure 1 (b) shows the parallel-to- \mathbf{B} profile of the normalized magnetic field strength B/B_0 actually used in this study. The parallel system length is set to be $L = 2.8$ m although it is much shorter than a real tokamak SOL-divertor system. The ratio of the maximum to the minimum magnetic field strength is $B_{\text{max}}/B_{\text{min}} = 2$. As boundary conditions, a mirror symmetry condition ($\partial n / \partial s = \partial T / \partial s = V = 0$) is imposed at the center $s/L = 0$ for simplicity and a sheath-edge condition is set at the target $s/L = 1$. In order to examine the viscosity behavior excluding the source effect, localized source terms for particle, S , and energy, Q_i and Q_e , are artificially given in proportion to $\exp[-20(s/L)^2]$. The ion heat source Q_i is kept to have the same value as the electron one Q_e and is divided into $Q_{i,\parallel} = Q_i/3$ and $Q_{i,\perp} = 2Q_i/3$ assuming isotropic heat sources for the AIP model. The momentum source M_m is set to be zero. The absolute values of source terms are changed in order to control the plasma collisionality which is estimated by L/λ_{mfpl} (λ_{mfpl} represents the mean free path of ion-ion Coulomb collisions) just in front of the sheath by the AIP model in this study. Deuterium is chosen as the ion species.

3 Results

Direct comparisons of plasma parameter profiles between the B2 code and the AIP model are shown in Figs. 2 and

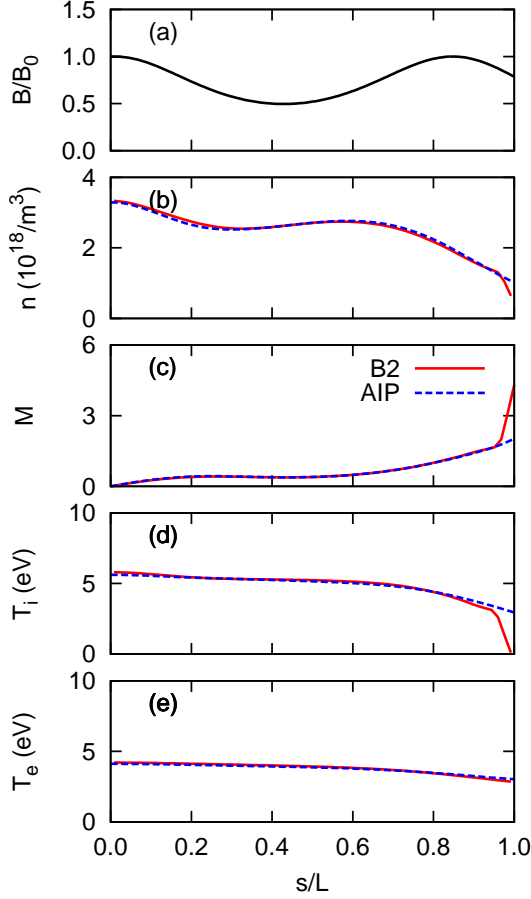


Fig. 2 Parallel-to- \mathbf{B} profiles of (a) normalized magnetic field B/B_0 , (b) plasma density n , (c) Mach number M , (d) ion temperature T_i and (e) electron temperature T_e of the B2 code (solid lines) and the AIP model (broken ones) for a collisional plasma ($L/\lambda_{\text{mfp}} \approx 20$).

3 for collisional ($L/\lambda_{\text{mfp}} \approx 20$) and collisionless ($L/\lambda_{\text{mfp}} \approx 0.2$) plasmas, respectively. Here, in estimating the Mach number M profiles, the parallel temperature $T_{i,\parallel}$ is used for the ion sound speed as $c_s \equiv \sqrt{(T_{i,\parallel} + T_e)/m_i}$ in the AIP model while $c_s \equiv \sqrt{(T_i + T_e)/m_i}$ is used in the B2 code.

In the collisional case, Fig. 2, a fairly good agreement between two models is obtained in all plasma parameters except for the vicinity of the target. A supersonic flow due to a magnetic nozzle [16] in the diverging-magnetic-field (DMF) divertor region $s/L > 0.85$ is obtained in both models. The deviation in the vicinity of the target might come from the different treatments of the Bohm criterion at the sheath entrance.

In the collisionless case, Fig. 3, on the other hand, a clear deviation is seen in the upstream DMF region in profiles of n and M in addition to the vicinity of the target. Because the temperature profiles are almost the same in the upstream DMF region, it is presumed that the parallel viscosity approximation of the anisotropic part of the ion pressure is responsible for this deviation.

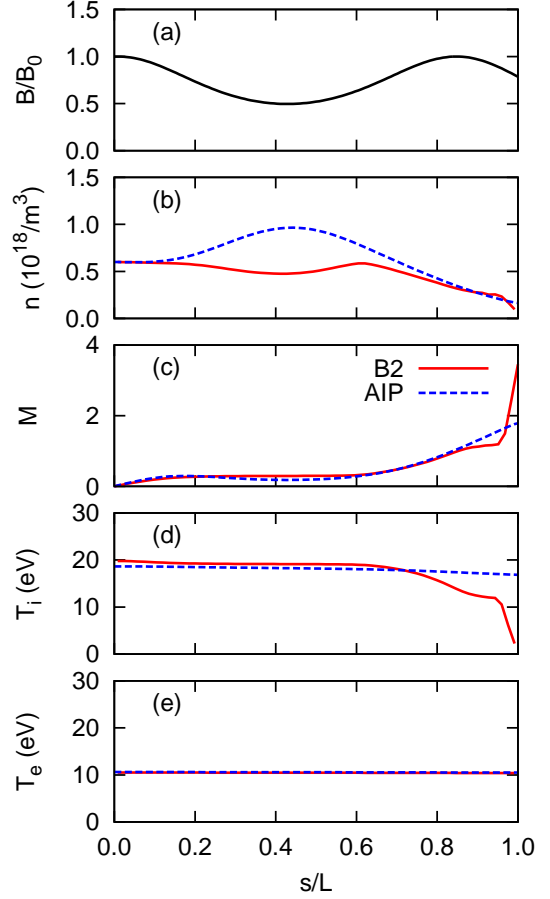


Fig. 3 Parallel-to- \mathbf{B} profiles of (a) normalized magnetic field B/B_0 , (b) plasma density n , (c) Mach number M , (d) ion temperature T_i and (e) electron temperature T_e of the B2 code (solid lines) and the AIP model (broken ones) for a collisionless plasma ($L/\lambda_{\text{mfp}} \approx 0.2$).

4 Discussion

By combining Eqs. (1)-(4), we derive the following generalized expression for the viscous flux;

$$\begin{aligned}
 & (1 + \Omega_\eta^{\text{gen}}) \delta p_i \\
 &= -\eta^{\text{gen}} B^{-1/2} \frac{\partial}{\partial s} (B^{1/2} V) \\
 &+ \eta^{\text{gen}} \frac{3V}{4p_i} \left(m_i n V \frac{\partial V}{\partial s} + \frac{\partial p_i}{\partial s} + \frac{\partial p_e}{\partial s} \right) \\
 &- \eta^{\text{gen}} \frac{1}{2p_i} \frac{\partial}{\partial s} (2q_{i,\parallel} - q_{i,\perp}) \\
 &- \eta^{\text{gen}} \frac{2q_{i,\perp} - q_{i,\parallel}}{Bp_i} \frac{\partial B}{\partial s} \\
 &+ \frac{5}{9} \tau_{\text{rlx}} m_i V^2 S - \frac{7}{9} \tau_{\text{rlx}} V M_m \\
 &+ \frac{2}{9} \tau_{\text{rlx}} (2Q_{i,\parallel} - Q_{i,\perp}),
 \end{aligned} \tag{10}$$

$$\eta^{\text{gen}} = \frac{10}{9} p_i \tau_i \approx \eta_{\text{cl}}, \tag{11}$$

$$\Omega_\eta^{\text{gen}} = \frac{\eta^{\text{gen}}}{(4/7) p_i} \frac{\partial V}{\partial s} + \frac{\eta^{\text{gen}} V}{8Bp_i} \frac{\partial B}{\partial s} + \frac{2m_e}{3m_i} \frac{\tau_{\text{rlx}}}{\tau_e}, \tag{12}$$

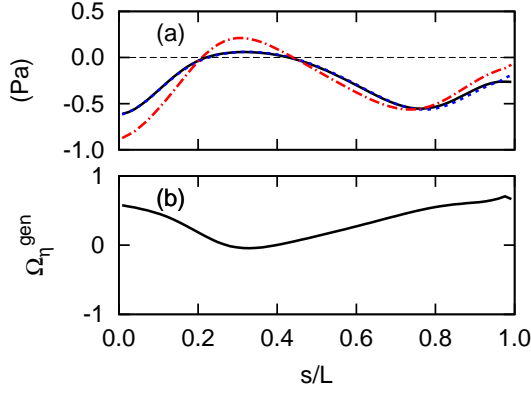


Fig. 4 Parallel-to- \mathbf{B} profiles of (a) $(1 + \Omega_{\eta}^{\text{gen}}) \delta p_i$ (solid line), the RHS of Eq. (10) (broken line), π_i^{gen} (chain line) and (b) $\Omega_{\eta}^{\text{gen}}$ for the collisional case.

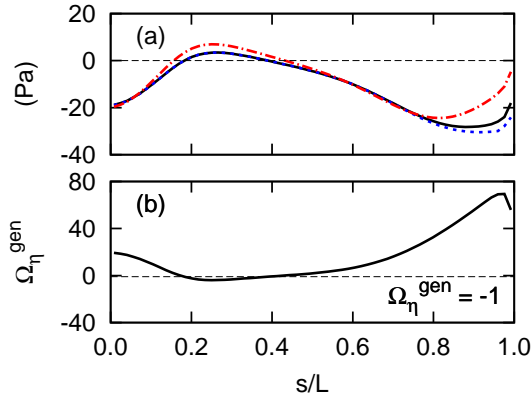


Fig. 5 Parallel-to- \mathbf{B} profiles of (a) $(1 + \Omega_{\eta}^{\text{gen}}) \delta p_i$ (solid line), the RHS of Eq. (10) (broken line), π_i^{gen} (chain line) and (b) $\Omega_{\eta}^{\text{gen}}$ for the collisionless case.

in which the steady state ($\partial/\partial t = 0$) is assumed. Note that the second and third terms in $\Omega_{\eta}^{\text{gen}}$ are much smaller than the first term and unity, respectively, and are negligible. Therefore, the essential difference of $\Omega_{\eta}^{\text{gen}}$ from Ω_{η} is that the absolute value of the flow velocity gradient, $|\partial V/\partial s|$, is not used. Note also that the first term in the RHS of Eq. (10), which is denoted by π_i^{gen} hereafter, has almost the same form as π_i .

In Fig. 4 (a), profiles are shown of $(1 + \Omega_{\eta}^{\text{gen}}) \delta p_i$, the RHS of Eq. (10) and π_i^{gen} estimated in the AIP model for the collisional case. It shows that the RHS of Eq. (10) agrees well with $(1 + \Omega_{\eta}^{\text{gen}}) \delta p_i$ (i.e. Eq. (10) is satisfied) and π_i^{gen} qualitatively approximates the behavior of $(1 + \Omega_{\eta}^{\text{gen}}) \delta p_i$. In this case, $\Omega_{\eta}^{\text{gen}}$ is positive or at least close to zero as shown in Fig. 4 (b) and, thus, $\Omega_{\eta} \approx \Omega_{\eta}^{\text{gen}}$ holds. Therefore, π_i in the B2 code approximates δp_i well in this case leading to a good agreement with the AIP model.

Figure 5 shows the same kinds of profiles as Fig. 4 for the collisionless case. It again shows that π_i^{gen} qualitatively approximates the behavior of $(1 + \Omega_{\eta}^{\text{gen}}) \delta p_i$. In this case,

however, $\Omega_{\eta}^{\text{gen}}$ becomes smaller than -1 in $0.2 \leq s/L \leq 0.4$ as shown in Fig. 5 (b). It means that the effective parallel-ion viscosity $\eta_{\text{eff}}^{\text{gen}} = \eta^{\text{gen}} (1 + \Omega_{\eta}^{\text{gen}})^{-1}$ to reproduce the behavior of δp_i in this region becomes negative which is physically unstable. Therefore, by using the absolute value of the flow velocity gradient, $|\partial V/\partial s|$, in estimating the effective parallel-ion viscosity as is done in the B2 code, Eq. (8), the problem becomes solvable. In this case, however, the validity of the viscosity approximation is lost leading to deviated profiles of plasma parameters from those from the AIP model as shown in Fig. 3.

The deviation in the density profiles in the upstream region as shown in Fig. 3 could lead to a difference in the amount of the total radial particle diffusive flux in a real situation and, thus, the particle flux onto the divertor plate can be different affecting the condition of the detached plasma. Therefore, $\Omega_{\eta}^{\text{gen}} > -1$ can be an important criterion in order to reproduce the behavior of detached plasmas with the Braginskii model.

Acknowledgement

Authors would like to thank Dr. D. Reiser of the Forschungszentrum Jülich GmbH for fruitful discussion.

References

- [1] R. Schneider *et al.*, Contrib. Plasma Phys. **46** (2006) 3.
- [2] H. Kawashima *et al.*, Plasma Fusion Res. **1** (2006) 031.
- [3] K. Shimizu *et al.*, Nucl. Fusion **49** (2009) 065028.
- [4] T. D. Rognlien *et al.*, J. Nucl. Mater. **196-198** (1992) 347.
- [5] A. V. Chankin *et al.*, J. Nucl. Mater. **390-391** (2009) 319.
- [6] K. Hoshino *et al.*, J. Plasma Fusion Res. Ser. **9** (2010) 592.
- [7] S. I. Braginskii, Reviews of Plasma Physics, vol. **1**, Consultants Bureau, New York, 1965, p. 205.
- [8] W. Fundamenski, Plasma Phys. Control. Fusion **47** (2005) R163.
- [9] S. Togo *et al.*, *submitted to* Contrib. Plasma Phys.
- [10] S. Togo *et al.*, 16th International Workshop on Plasma Edge Theory in Fusion Devices (2017) O-05.
- [11] S. Togo *et al.*, Contrib. Plasma Phys. **56** (2016) 729.
- [12] E. Zawaideh *et al.*, Phys. Fluids **29** (1986) 463.
- [13] S. Togo *et al.*, J. Nucl. Mater. **463** (2015) 502.
- [14] S. Togo *et al.*, J. Comput. Phys. **310** (2016) 109.
- [15] B. J. Braams, NET report no. 68 (EUR-FU/XII-80/87/68) (1987).
- [16] R. H. Cohen and D. Ryutov, Contrib. Plasma Phys. **44** (2004) 111.

Simulation study of vapor shielding at a solid wall by a weighted PIC method

K. Ibano^{1*}, A. Tanaka¹, Y. Kikuchi², S. Togo³, H. T. Lee¹, Y. Ueda¹, and T. Takizuka¹

¹ Graduate school of Engineering, Osaka University, Suita 565-0871 Japan

² Graduate school of Engineering, University of Hyogo, Himeji 671-2280 Japan

³ Plasma Research Center, University of Tsukuba, Tsukuba, Japan

Introduction

When the plasma facing surface suffers intense plasma loads, vaporized wall material interacts with the incoming plasma flux and “shields” the remaining wall. This phenomena is known as vapor shielding and now interests are being increased as an inherent mitigation [1–5]. In particular, transient heat loads in ITER are expected to be considerably larger than ones in current devices [6], e.g., edge localized mode (ELM) can reach 0.1~1 GW/m² for 0.1~1 ms. If the vapor shielding effectively mitigate the plasma energy, less amounts of heat loads are absorbed to the wall. In case of the vapor shielding at a solid wall, several physical phenomena occur; melting of the surface, molten layer instability, droplet ejections, vapor emission and their ionization. Thus, there are multiphase matters, i.e., plasma, gas, liquid, and solid phases and their interactions. Effects of these reactions are examined previously by analytic modeling [7] and simulation works [8,9]. MHD fluid modeling were applied for these simulation works. In the fluid model, the boundary conditions are usually set on a plasma-sheath entrance. However, the vapor shielding happens mainly in vicinity of a surface, and the reactions in the sheath region should be solved. Thus, we employ a Particle-In-Cell (PIC) simulation. In the PIC simulation, kinetic behaviors of super particles are solved. The super particles are computation particle which represents numbers of real particles. Then, the PIC can simulate the particle behavior in the sheath region. The simulation model is further described in the next section. In order to validate our simulation code, a comparison is taken with experimental observation from a plasma gun (PG); observation of vapor shielding at a helium plasma irradiation on an Al coated W specimen. Heat flux dissipation in the PG was observed for the Al coated W specimen due to the expanding Al clouds.

Model Description

In this study, a PIC code, named PIXY[10,11], is applied for the simulation. The PIXY code solves trajectories of all particles (ions, electrons, and impurities) for 1 dimension in space and 3 dimensions in velocity (1d3v). Magnetic pre-sheath and Debye sheath can be simulated with this coordination. In the 1d simulation space, central region is set as a Langevin heat bath region where electrons and ions are supplied. The super particles move toward the boundary of the system. As they reached to the boundary, their energy is counted as the heat flux to the wall. Then, a heat transfer calculation is taken for the wall component using the heat flux as a surface boundary by solving a 1d heat transfer equation. The heat transfer calculation determines the surface temperature, then evaporation rate of surface materials is determined. These evaporated particles are fed into the plasma side. The interaction between the ejected vapor particles and incoming plasma are also solved. Several Atomic and Molecular reactions are treated by Monte-Carlo techniques; ionization, recombination, and radiations via line, Bremsstrahlung, and recombination. Probabilities of these reactions in a time-step are calculated based on their reaction rates in the OPEN-ADAS database [12] and compared with a random-number. When the reaction happens, corresponding energy balance is maintained by loss or gain of a randomly-selected electron in a same cell. As well as the A&M reactions, ion-neutral collision is also simulated by a Monte-Carlo method. The ion-neutral elastic cross sections are calculated from the semi-classical approximation explained in [13] where the dipole polarizability is taken from ref [14]. Once reaction is determined via a comparison between the reaction rate and a random number for a neutral particle, an ion in a same cell is randomly selected as a binary collision partner. In order to avoid over counting of this collision effects, trajectories of neutral particles are calculated in a three-dimensional space. Then, if neutral particles leave from a plasma tube, they are counted as pumped out. In the Plasma Gun simulation, a 10 cm diameter plasma tube is used as the boundary.

* Corresponding author. E-mail: kibano@eei.eng.osaka-u.ac.jp, Phone: +81 6 6879 7234, Fax: +81 6 6879 7867

One issue is vapor ejection rate which changes significantly with surface temperature. If same super particle weights (number of particles represented by a super particle) are used throughout the calculation, numbers of super particles become significantly large. Thus, we use the weighted particle model. In this model, particle weights are different for all super particles. Then, the significant difference in emission rates of impurity particles can be treated.

Results

In the plasma gun, vapor shielding by Al vapor cloud was observed in a helium plasma gun irradiation onto an Al coated W specimen. The typical plasma parameters of the plasma gun are; electron temperature $T_e \sim 30$ eV, density $n_e \sim 10^{21} \text{ m}^{-3}$, and energy density 1 MJ/m^2 for 0.2 ms. The detail of the PG experiment can be found in ref. [15,16]. The specimen was a thin W specimen with a thickness of $50 \mu\text{m}$ coated by an Al thin layer with a thickness of $3 \mu\text{m}$. Specimen temperature was monitored by a pyrometer to the back surface. Steady-state temperature of the W and Al/W specimens after the shots were 2250 K and 1600 K, respectively. In the plasma gun simulation, the plasma with the 30 eV and $3 \times 10^{21} \text{ m}^{-3}$ is simulated. As Al ejection starts, excitation, recombination and Bremsstrahlung radiation are observed. Then, as the PG pulse fully develops and reaches to the specimen, massive evaporation of Al due to the ablation starts. Increasing radiation due to larger Al density dissipates the incoming plasma energy, then a temperature drop near specimen is observed. Finally, the Al clouds expands to the entire calculation region and the PG plasma energy is effectively dissipated.

Simulated temporal change of the heat flux q'' during the pulse is shown in Fig. 1. Developing heat flux as the PG plasma reaches to the steady states is seen until $20 \mu\text{s}$ after the pulse starts. Strong drop of heat flux is seen at $100 \mu\text{s}$. In contrast, PG heat flux to the W specimen keeps constant during the PG pulse. The heat flux dissipation is well seen from this result. A remarkable heat flux dissipation of ions due to ion-neutral collision, which is comparable to the radiation cooling without radiation trapping, is observed. Thus, although the radiation transport and trapping models need to be included for the precise heat flux estimation, it can be concluded that the ion-neutral collision is also important during the vapor shielding as well as the radiation cooling on electrons.

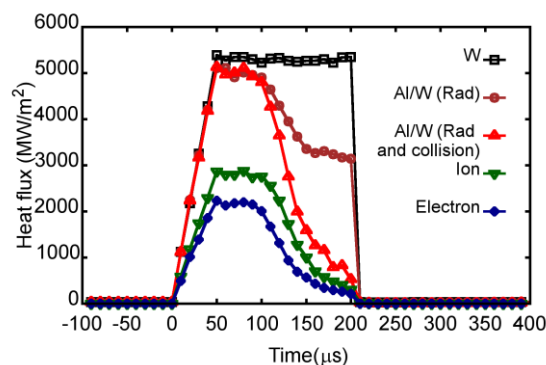


Figure 1 Temporal change of heat flux during the plasma gun pulse for the plane W and the Al coated W specimens. Individual heat flux for the Al coated W specimen with ion-neutral collision model is also shown.[17]

Summary

A weighted PIC code, PIXY, is applied for simulations of heat flux dissipation by vapor from a solid wall (vapor shielding) observed at the plasma gun experiments using an Al coated W specimen. In the simulation, 1d3v PIC model including various A&M reactions combined with a heat transfer calculation at the wall is used. The weighted particle method is applied to treat the vapor emission flux largely varied by the wall temperature. The plasma gun pulse was well simulated by the code and energy dissipation was reproduced.

* Corresponding author. E-mail: kibano@eei.eng.osaka-u.ac.jp, Phone: +81 6 6879 7234, Fax: +81 6 6879 7867

It was found that the ion-neutral collision as well as the radiation cooling is the important reactions for the energy dissipation at the vapor shielding.

Acknowledgements. This work is performed on "Plasma Simulator" (FUJITSU FX100) of NIFS with the support and under the auspices of the NIFS Collaboration Research program (NIFS16KNXN320). This work is partially supported by the "ZE Research Program, IAE ZE29B-01".

References

- [1] J.K. Tripathi, T.J. Novakowski, G. Joseph, et al., *J. Nucl. Mater.* 464 (2015) 97–106.
- [2] T. Sizyuk, A. Hassanein, *Nucl. Fusion.* 54 (2014) 23004.
- [3] Y. Kikuchi, I. Sakuma, Y. Kitagawa, et al., *J. Nucl. Mater.* 463 (2015) 206–209.
- [4] G.G. van Eden, T.W. Morgan, D.U.B. Aussems, et al., *Phys. Rev. Lett.* 116 (2016) 135002.
- [5] G.G. van Eden, V. Kvon, M.C.M. van de Sanden, et al., *Nat. Commun.* 8 (2017) 192.
- [6] G. Federici, A. Loarte, G. Strohmayer, *Plasma Phys. Control. Fusion.* 45 (2003) 1523–1547.
- [7] D.I. Skovorodin, A.A. Pshenov, A.S. Arakcheev, et al., *Phys. Plasmas.* 23 (2016) 22501.
- [8] H. Wurz, I. Landman, B. Bazylev, et al., *J. Nucl. Mater.* 233 (1996) 798–802.
- [9] A. Hassanein, *Fusion Eng. Des.* 60 (2002) 527–546.
- [10] K. Ibano, D. Nishijima, J.H. Yu, et al., *Nucl. Mater. Energy.* 12 (2016) 278–282.
- [11] K. Ibano, S. Togo, T.L. Lang, et al., *Contrib. Plasma Phys.* 56 (2016) 705–710.
- [12] H.P. Summers, M.G. O'Mullane, Atomic data and modelling for fusion: The ADAS Project, in: *AIP Conf. Proc.*, 2011.
- [13] C.H. Liu, J.G. Wang, R.K. Janev, *J. Phys. B At. Mol. Opt. Phys.* 43 (2010) 144006.
- [14] P. Schwerdtfeger, *Table Exp. Calc. Static Dipole Polariz.* [online] (2015).
<http://ctcp.massey.ac.nz/dipole-polarizabilities>.
- [15] I. Sakuma, Y. Kikuchi, Y. Kitagawa, et al., *J. Nucl. Mater.* 463 (2015) 233–236.
- [16] I. Sakuma, Y. Kikuchi, W. Isono, et al., *Plasma Fusion Res.* 10 (2015) 1205089.
- [17] K. Ibano, Y. Kikuchi, A. Tanaka, et al., *Contrib. to Plasma Phys.* to be published

Simulation for stability of di-vacancy in tungsten

Kazuhito Ohsawa¹, Ken Toyama², Yuji Hatano³, Masatake Yamaguchi⁴, Hideo Watanabe¹

¹Research Institute for Applied Mechanics, Kyushu University

²Institute for Materials Research, Tohoku University

³Hydrogen Isotope Research Center, University of Toyama

⁴Center for Computational Science and e-system, Japan Atomic Energy Agency

1. Introduction

Divertor armor tiles installed in fusion reactors are exposed to intense plasma particle irradiation. So, it is planning that the divertor armor tiles are covered by tungsten (W) or its alloys because they have excellent properties as plasma facing materials (PFMs), e.g., low hydrogen (H) solubility, high melting point and high thermal conductivity etc. However, a large amount of H isotope retention has been reported in the W materials. In particular, tritium (T) inventory is an important subject associated with safety of fusion reactors. Usually, H isotopes are not retained in W crystal lattice because of its low H solubility and large diffusivity. However, H isotopes are accommodated in irradiated zone of the W materials. Vacancy-type lattice defects and impurities are supposed to be plausible trap sites for the H isotopes [1].

In the present report, we pay attention to stable configuration of di-vacancy in W lattice and other BCC transition metals for comparison. Besides, we investigate the effect of H presence on the di-vacancy stability in those transition metals. Di-vacancies in metals are usually stable. But formation energy of di-vacancy, i.e., binding energy of two vacancies, in W is estimated to be negative [2]. So, it is expected that di-vacancy nucleation does not occur in W. On the other hand, the presence of H or H isotopes will enhance the growth of vacancy-type lattice defects.

Positron annihilation lifetime measurement is effective method to observe vacancy-type lattice defects in metals. So, we calculate the positron lifetime to examine di-vacancy formation in W.

2. Computational method

Binding energy of two vacancies for di-vacancy formation and binding energy of vacancy-hydrogen complexes are defined in Eq. (1) and (2), respectively.

$$E_B = 2E[V] - E[V_2] \quad (1)$$

$$E_B = E[VH_m] + E[VH_n] - E[V_2H_{m+n}], \quad (2)$$

where V and H represent vacancy and hydrogen atom, respectively. Therefore, V_2 indicates di-vacancy and VH_m represents vacancy-hydrogen complex trapping m hydrogen atoms in a vacancy. Similarly, V_2H_{m+n} indicates that di-vacancy trapping $m+n$ hydrogen atoms. The function E is the cohesive energy of the system including such lattice defects. Positive binding energy corresponds to attractive interaction between the lattice defects. The cohesive energies are calculated in terms of first-principle calculations on the basis of density functional theory. The calculations are performed by using Vienna ab initio simulation package (VASP) with PBE type potential. The cut-off energy of plane wave is 350eV. We used large simulation cell composed of 432 lattice points (6x6x6 BCC lattice) in the present calculations in order to reduce the artificial effects of periodic boundary condition imposed in the simulation cell. Lattice relaxations are iterated until resultant force of each atom is lowered than 0.003 eV/Å.

Positron lifetime τ is estimated in the overlap integral

$$\tau^{-1} = \pi c a_0^2 \int_V n_+(\vec{r}) n_-(\vec{r}) g(n_+ n_-) d\vec{r} \quad (3)$$

where n_+ and n_- are positron and electron charge densities, respectively. The constants a_0 and c are classical radius of electron and light velocity, respectively. In the present calculation, the enhancement factor $g(n_+ n_-)$ in Eq. (3) is estimated from positron lifetime measured from bulk W experimentally. The electron charge density around W atom is given from reference [3].

3. Results

Two types of configurations are possible for di-vacancy in BCC lattice, that is, the two vacancies line up in the $\langle 111 \rangle$ or $\langle 100 \rangle$ direction. We calculate binding energies of two vacancies in a variety of BCC transition metals in Eq. (1). $\langle 111 \rangle$ arrangement of two vacancies is stable in V (vanadium), Cr, Mo, and W, while $\langle 100 \rangle$ arrangement is favorable in Fe, Nb and Ta. In addition to it, binding energies of vacancy-hydrogen complex VH_6 are also calculated in Eq. (2). Fig. 1 shows the binding energies of two vacancies for di-vacancy formation and binding energies of VH_6 for V_2H_{12} formation in the BCC metals. Fig. 2 shows binding energies of VH_n in W in detail, where $n=0, 1, 2, 3,$ and 6 in the present work. These calculations indicate that di-vacancy is usually stable than isolated two vacancies in BCC transition metals. However, binding energy of two vacancies in W is negative. So, di-vacancy in W is only unstable. Besides, the presence of H atoms contributes to stabilization of the di-vacancy.

Lifetime of positron trapped in di-vacancy is calculated in Eq. (3). Positron lifetime in bulk W lattice is experimentally measured as 118 ps [4]. According to it, the enhancement factor $g(n_+, n_-)$ in Eq. (3) is estimated to be 1.91. So, lifetime of positron trapped in di-vacancy introduced in W lattice is estimated to be 210 ps, which is good agreement of experimental results.

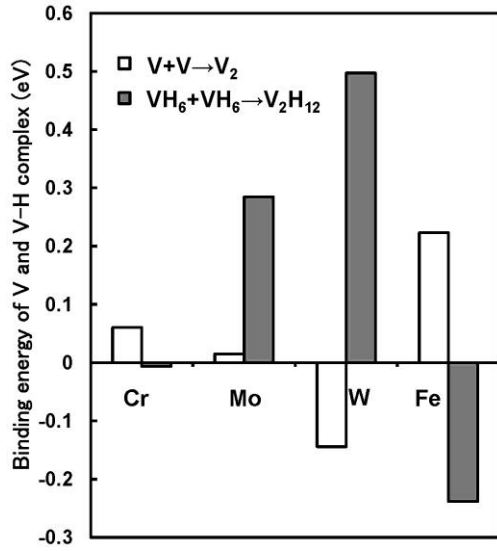


Fig. 1: Binding energies of vacancies and vacancy-hydrogen complexes in BCC metals.

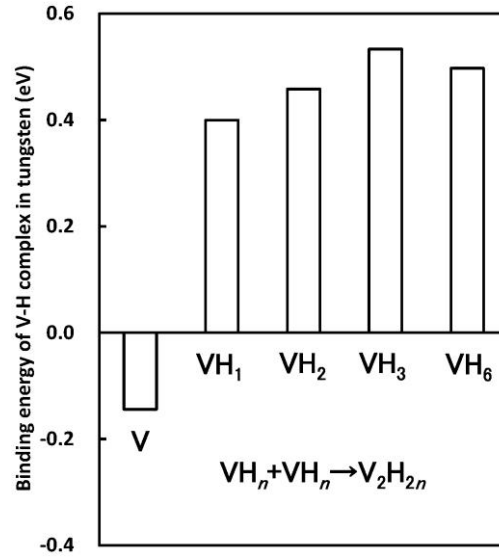


Fig. 2: Binding energies of a variety of vacancy-hydrogen complexes in W.

4. Discussion

Vacancy cluster growth and the following void swelling is one of the troublesome phenomena for metals in irradiation circumstance, which causes degradation of structural materials. If formation energies of vacancy-type lattice defects are assumed to be proportional to the surface area of the defects, vacancy cluster growth will occur so as to reduce the formation energies. Actually, di-vacancy is more stable than isolated two vacancies in many kinds of metals, as shown in Fig. 1. However, di-vacancy in W is unstable exceptionally, according to the present calculations. On the other hand, the presence of H and H isotopes contribute to binding of vacancies in W and other BCC transition metals. Therefore, we infer that di-vacancy formation does not occur in annealing process in W specimen even if sufficiently high density vacancies are introduced in the W specimen. On the other hand, the presence of H and H isotopes will enhance the growth of vacancy-type defects, as shown in Fig. 3. Hydrogen plasma and irradiation circumstance coexist in fusion reactors. Therefore, the influence of H on such vacancy-type lattice defects is one of the important subjects in the field of PFM.

Positron annihilation measurement in Fig. 4 is a sensitive experimental method to investigate the structure of vacancy-type lattice defects in metals. The size of vacancy-type lattice defect is reflected to the positron lifetime. Usually, di-vacancy formation in metals is proved by drastic extension of the positron lifetime at vacancy diffusion temperature in annealing process. We hope that the behaviors of vacancies in W specimen will be revealed by the positron annihilation measurement.

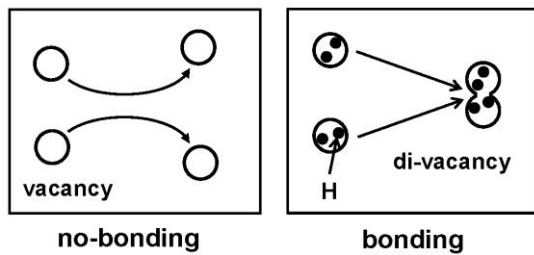


Fig. 3: Schematic view of bonding of vacancy and vacancy-hydrogen complex in W specimen. It is expected that di-vacancy formation does not occur in W.

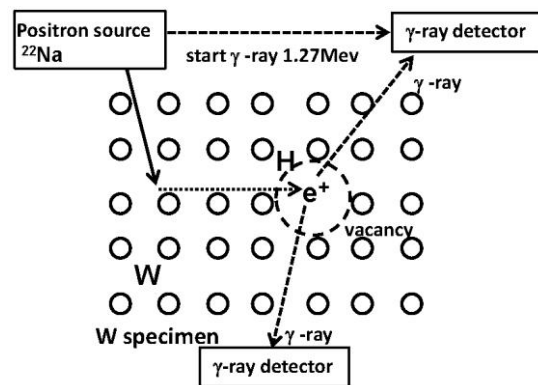


Fig.4: Schematic view of the positron annihilation lifetime measurement.

Acknowledgement

This work was supported by JSPS KAKENHI Grant Number 17K06993, and the collaboration programs of Research Institute for Applied Mechanics, Kyushu University and Hydrogen Isotope Research Center, Organization for Promotion Research, University of Toyama.

References

- [1] K. ohsawa *et al.*, Phys. Rev. B 85 (2010) 184117.
- [2] L. Ventelon *et al.*, J. Nucl. Mat. 458 (2015) 187.
- [3] F. Herman *et al.*, *Atomic Structure Calculations*, Prentice-Hall Inc. (1963).
- [4] T. Toyama *et al.* J. Nucl. Mater. 499 (2018) 464.

Application of Genetic Algorithms to Modeling of Plasma Physics

M. Honda

*National Institutes for Quantum and Radiological Science and Technology, Naka,
Ibaraki 311-0193 Japan*

Introduction

The genetic algorithm (GA) based optimizer is a powerful tool for global optimization, such as finding a global maximum, not local maxima, which are typically more than a gradient-based method can manage. Sometimes it is advantageous compared to other schemes with respect to the convenience, partly because a merit function is not necessarily differentiable. Taking advantage of this feature, it is applied to physical modelings of magnetically confined toroidal plasmas. Here, we show some examples such as searching the positions of the magnetic axis and fitting an analytic function to the measurement points. Through the modelings, the wide applicability of the genetic algorithm based optimizer is elucidated.

Genetic Algorithms

GAs are a class of metaheuristics inspired by the evolutionary biology. GAs make use of the ideas of the evolutionary biology such as the natural selection, inheritance and variability and turn them into the algorithm suited for computational calculations. GAs are commonly used to robustly generate solutions to optimization and search problems and, as such, they are known as GA-based optimizers. A GA-based optimizer has the advantage in that it is applicable to global and multi-dimensional problems and does not require a fitness function to be differentiable. By contrast, it is computationally slower than other typical algorithms that can be applied to global problems and local optimization methods. Capability of a global optimization is traded off for a slow computation. In this paper, the public domain GA package PIKAIA [1, 2] is used as a GA-based optimizer.

Searching the magnetic axis

Searching a magnetic axis of an axisymmetric equilibrium in tokamaks computed by a Grad-Shafranov solver is a sort of global optimization problem. Equilibria we use are adjusted such that ψ on the outermost nested closed flux surface becomes zero and the contour is concave upward, and thus the magnetic axis is the point where ψ becomes negative maximum. Hence, the magnetic axis may be located at \mathbf{x} where the fitness function, $f(\mathbf{x}) = -\psi$ for $\mathbf{x} = (R, Z)$, is maximized. Namely, an individual has the information of the position in the domain and the corresponding ψ can be evaluated

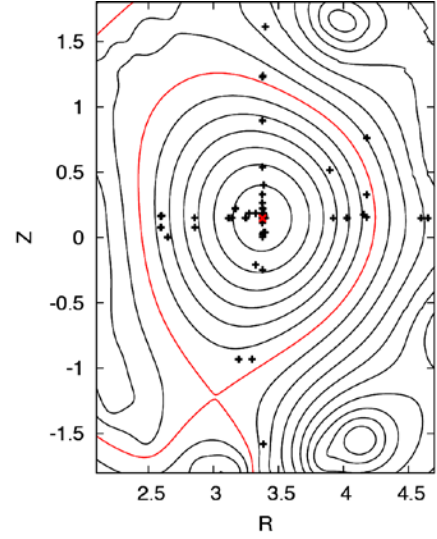


Fig. 1: Searching the magnetic axis. The black crosses are the individuals at the 20th generation and the red \times mark is the fittest one.

as the fitness. An evolutionary run is carried out over 200 generations and the population size is 100. The snapshots of the evolutionary runs at the 20th generation are shown in Fig. 1 for the normal magnetic shear plasma. The majority of the individuals is confined inside the plasma at this stage. Until around 30 generation, the fittest individual reaches the magnetic axis.

Profile fitting

We now attempt to fit a given function through the discrete measurement data in terms of the density and temperature profiles. The double transport barrier formation has been often achieved in JT-60U, which means that the edge and internal transport barriers are simultaneously formed. In such cases, it is too difficult to use a polynomial function for profile fitting due to Runge's phenomenon, as discussed in Introduction. To fit such data, the model would take the form:

$$g(\rho; \mathbf{x}) = x_1 \tanh[-x_2(\rho - x_3)] + x_4 \tanh[-x_5(\rho - x_6)] + x_7$$

where the radial coordinate ρ is typically defined by the square root of the normalized toroidal magnetic flux and $\rho \in [0,1]$. The function g is infinitely differentiable with respect to ρ , a fact which makes it easy to use for numerical codes. The hyperbolic

tangent $\tanh \xi$ is suitable for expressing the sharp change in the profile by adjusting the position of $\xi = 0$ to that of transport barriers. Hence, the model consists of two hyperbolic tangent functions: one is for the ITB and the other is for the edge transport barrier (ETB). The position of the transport barrier almost corresponds to x_3 and x_6 , respectively. The steepness of a barrier is controlled by x_2 and x_5 . The factor x_7 is imperative for fitting. As readily seen from the form of g , solving the simultaneous equations after taking the derivative of g with respect to x may not be performed analytically and is very difficult even numerically. A GA-based optimizer is a powerful tool to tackle this sort of problems. The fitness function may be given as $f(\mathbf{x}) = \chi^2$ where $\chi^2 = \sum_i [(y_i - g(\rho_i; \mathbf{x})) / \sigma_i]^2$. Here, i denotes the index of a discrete set of the measurement points, y_i is a measured quantity and σ_i denotes the measurement error.

We now attempt to fit the measurement data of the electron and ion temperatures with the function g . An evolutionary run has been executed until the 500th generation and requires about 0.2 sec. It is obvious in Fig. 2 that the hyperbolic tangent functions play an important role in expressing the steep temperature gradient in both the core and edge of the plasma. The GA-based optimizer has revealed its capability in that one single function is able to fit the measurement points in a wide variety of discharges. The numerical implementation for fitting is rather simple and there is no need to compute the Jacobian by differentiating the function unlike the Gauss-Newton algorithm. Any function is of course applicable and one may seek the form of a model function, depending upon the situation.

References

- [1] P. Charbonneau, *Astrophys. J. Suppl. Ser.* 101 (1995) 309.
- [2] <http://www.hao.ucar.edu/modeling/pikaia/pikaia.php>

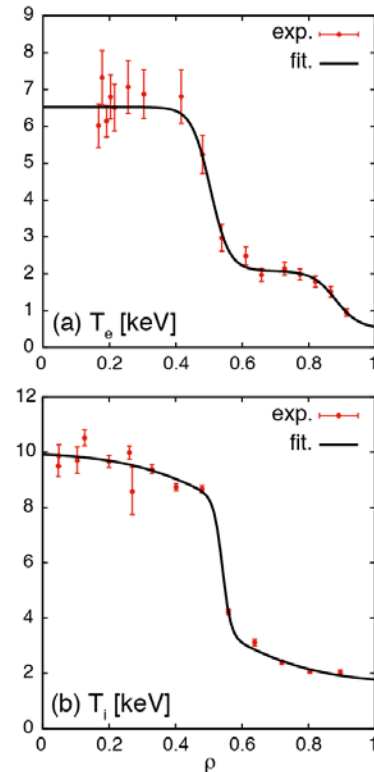


Fig. 2: Profile fitting of (a) the electron temperature and (b) the ion temperature for the box type ITB plasma.

Pattern selection in drift wave turbulence with parallel shear flow

Y. Kosuga^[1,2]

[1] Research Institute for Applied Mechanics, Kyushu University, Fukuoka, Japan

[2] Research Center for Plasma Turbulence, Kyushu University, Fukuoka, Japan

Convective cells - nonlinearly generated ExB vorticities - play important roles in the nonlinear dynamics of turbulent plasmas. As they are linearly unstable, convective cells are nonlinearly driven from primary drift wave turbulence. There are two important limits of convective cells. One is a radially elongated cell, which is called a streamer. The other is a poloidally elongated cells, and is called a zonal flow. Since streamer and zonal flow have different impact on turbulent transport, it is a critical issue to understand their selection rule[1].

In this work, we discuss the role of parallel shear flow on the selection of zonal flow and streamer in drift wave turbulence[2]. Employing a modulational instability model for secondary flow generation, we show that parallel shear flow enters as a critical parameter. Parallel shear flow modifies dispersion of underlying drift waves. This in turn leads to the enhancement/suppression of secondary flow response. As a result, shearing feedback on the background fluctuation envelope becomes a function of parallel flow shear. Though the modulational instability analysis, we show that there is a parameter window of parallel flow shear for streamers to be selected in the system.

Stimulating discussion with Drs. S.-I. Itoh, K. Itoh, S. Inagaki, T. Kobayashi, P.H. Diamond, L. Wang, and Z. Guo is acknowledged. This work was supported by Grants-in-Aid for Scientific Research of JSPF of Japan (JP15H02155, JP15K17799, JP17H06089), the Joint research project in RIAM.

References

- [1] S. Champeaux and P.H. Diamond, Phys. Lett. A **288** 214 (2001)
- [2] Y. Kosuga, Phys. Plasmas **24** 122305 (2017)

Enhancement and suppression of turbulence by energetic particle driven geodesic acoustic modes

M. Sasaki^{1, 2}

¹Research Institute for Applied Mechanics, Kyushu University, Kasuga 816-8580, Japan

²Research Center for Plasma Turbulence, Kyushu University, Kasuga 816-8580, Japan

1 Introduction

Problems on interactions between micro-turbulence and macro scale flows, such as zonal flows, are important subjects in magnetically confined plasmas [1]. In toroidal plasmas, geodesic acoustic modes (GAMs), which are oscillatory zonal flows driven by turbulence and/or by energetic particles, have attracted much attention, because GAMs are expected to suppress turbulence by their velocity shear. Actually, the suppression of turbulence and transport have been reported in turbulence simulations [2]. However, recently, the enhancement of turbulence by GAMs driven by energetic particles (which are called EGAMs) has been observed in gyrokinetic simulations, with the subsequent destruction of a transport barrier [3]. In this way, EGAMs can either mitigate or enhance the turbulence. This dual effect of the GAMs on turbulence requires theoretical investigation. In this study, we investigate the phase-space dynamics of spatially inhomogeneous turbulence in the presence of EGAMs. We show that EGAMs can carry clump of turbulence spatially, which leads to the enhancement of turbulence in the regions where the turbulence is stable, while the turbulence is suppressed in the region where the turbulence is unstable [4].

2 Model

In this study, we consider the dynamics of spatially inhomogeneous turbulence with a transport barrier in the presence of EGAMs. Details of the problem settings are written in [4]. We consider the drift wave type turbulence, which is governed by the wave-kinetic equation, and focus on the dynamics in the phase space, where the phase space consists of the real space, x (the radial direction in toroidal plasma) and the wavenumber k_x . The spatio-temporal behavior of the EGAM is given, and the time evolution of the turbulence in the phase space is numerically calculated based on the wave-kinetic equation.

3 Results

The snapshot of the turbulence action, N_k , in the phase space is shown in Fig. 1. In the case without EGAM, the intensity of the turbulence is large in the region where the turbulence is unstable, and only the turbulence with small k_x leaks into the stable region across the shear layer (transport barrier). On the other hand, clumps of turbulence can be seen in the stable

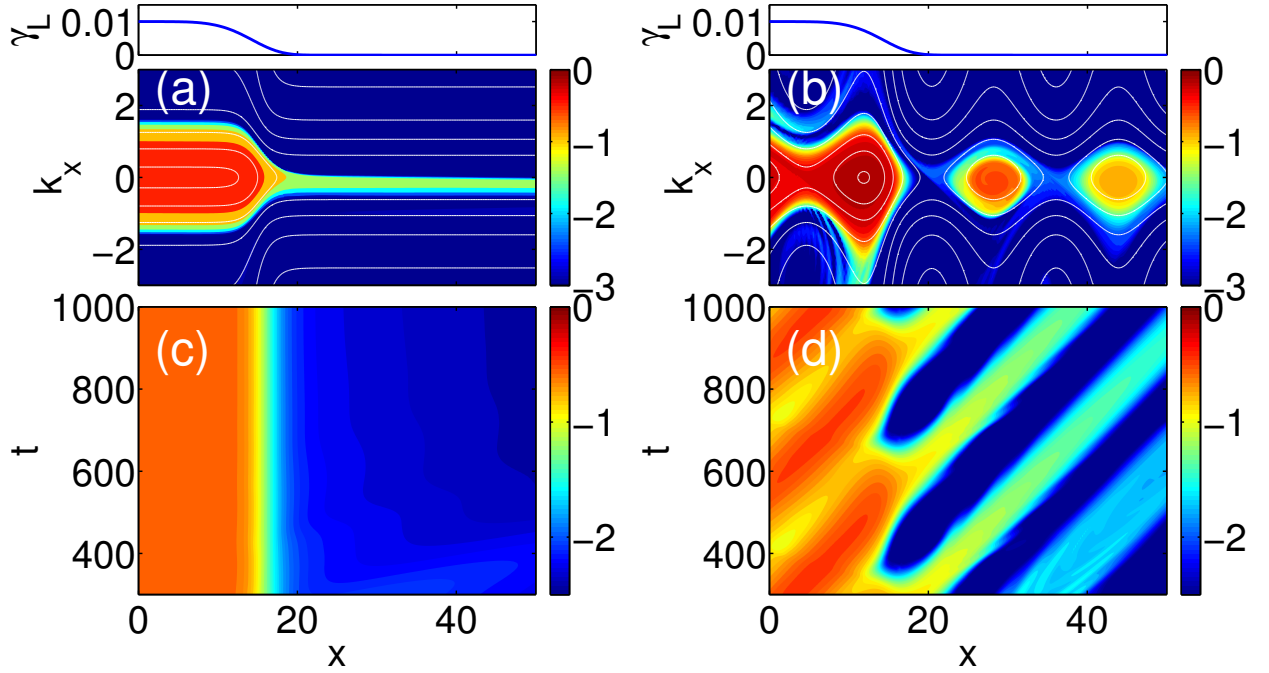


Fig. 1: Snapshots of N_k in the case of (a) $V_G = 0$, and (b) $V_G = 0.1$ are shown, where V_G is the amplitude of the EGAM. The time evolution of turbulence intensity is shown for the case of (c) $V_G = 0$, and (d) $V_G = 0.1$ [4].

region, when the EGAM amplitude becomes finite. The clump of turbulence propagates with the phase velocity of the EGAMs. This is due to the turbulence trapping [5] by the EGAM. We found that the trapped turbulence wave-packets leak across the transport barrier. As a result, turbulence is enhanced by EGAMs in the stable region, while turbulence suppression is obtained in the unstable region. The propagation of the turbulence is ballistic, with the phase velocity of the EGAM. Hence, there appear a new global characteristic velocity for turbulence dynamics, in addition to the local group velocity and that of the turbulence spreading [6]. This paper firstly shows that the turbulence trapping in the phase space strongly affects the turbulence profile in the real space, and that this effect can be a new mechanism of the turbulence propagation.

References

- [1] P. H. Diamond, et. al., Nucl. Fusion, **49**, 045002 (2009).
- [2] K. Hallatschek, D. Biskamp, Phys. Rev. Lett., **86**, 1223 (2001).
- [3] D. Zarzoso, et. al., Phys. Rev. Lett., **110**, 125002 (2013).
- [4] M. Sasaki, et. al., Scientific Reports, **7**, 16767 (2017).
- [5] P. Kaw, R. Singh, P. H. Diamond, Plasma Phys. Control. Fusion, **44**, 51 (2002).
- [6] O. D. Gurcan, et. al., Phys. Plasmas, **12**, 032303 (2005).

Global mode analysis of ion-temperature-gradient instabilities using the gyro-fluid model in linear devices

Tomotsugu OHNO¹, Naohiro KASUYA², Makoto SASAKI², Masatoshi YAGI³

1. Interdisciplinary Graduate School of Engineering Sciences, Kyushu University, 6-1 Kasuga-Koen, Kasuga, Fukuoka 816-8580, Japan

2. Research Institute for Applied Mechanics, Kyushu University, 6-1 Kasuga-Koen, Kasuga, Fukuoka 816-8580, Japan

3. National Institutes for Quantum and Radiological Science and Technology, 2-166 Omotedate, Obuchi, Rokkasho-mura, Aomori 039-3212, Japan

1. Introduction

It is important to understand turbulent phenomena in magnetically confined plasmas. A level of turbulent transport is determined by competition of several instabilities and formation of turbulent structures [1]. Fundamental mechanisms of structural formation in turbulent plasmas can be studied in simple cylindrical configurations [2]. One of the candidates to cause anomalous transport in fusion plasmas is the microscopic instability due to the ion temperature gradient (ITG) [3]. Studies of excitation conditions of the ITG instability have been carried out in basic experiments [4]. The ion temperature can be measured using diagnostics as an ion-sensitive probe [5]. On linear device PANTA [6], ion temperature measurements and numerical analyses of the ITG instability have been progressing. The purpose of our research is to predict excitation conditions of the ITG instability in PANTA. The ITG instability is predicted to be excited when the ratio of the ion temperature gradient to the density gradient exceeds the threshold value near the unity [7]. Numerical simulations by using the fluid model in PANTA shows that a mode with $k_{\perp}\rho_s \sim 1$ can become unstable even in low ion temperature plasmas as in linear devices. Here, k_{\perp} and ρ_s are the wavenumber in the perpendicular direction to the magnetic field and the effective Larmor radius, respectively. Therefore, a detailed analysis including the finite Larmor radius (FLR) effect is required. Analyses using a set of localized gyro-fluid equations have been carried out [8]. The ion Larmor radius is not much smaller than the plasma radius in the linear device, so the global mode structure must be calculated. In this research, a numerical simulation code is developed to solve global eigen-functions of the ITG instability with the gyro-fluid model. Here we report mode structures and parameter dependences of the ITG instability in PANTA by using the global code.

2. Global Mode Analysis

2.1 Gyro-Fluid Model

A set of gyro-fluid equations is derived by taking the moments of the electrostatic gyro-kinetic equation in the velocity spaces [9]. The target plasma has a cylindrical configuration with a homogeneous magnetic field parallel to the axial direction, so the magnetic curvature terms can be eliminated. Applying the gyro-kinetic ordering, the linear forms of the equations in the cylinder are given to be

$$\frac{dn}{dt} + \nabla_{\parallel} u_{\parallel} + \left(1 + \eta_{\perp} \frac{\hat{\nabla}_{\perp}^2}{2}\right) \frac{\rho_s}{L_n} \frac{\partial \Psi}{\partial y} = 0, \quad (1) \quad \frac{du_{\parallel}}{dt} + \nabla_{\parallel} (\tau n + T_{\parallel} + \Psi) = 0, \quad (2)$$

$$\frac{1}{\tau} \frac{dT_{\parallel}}{dt} + \nabla_{\parallel} (2u_{\parallel} + q_{\parallel}) + \eta_{\parallel} \frac{\rho_s}{L_n} \frac{\partial \Psi}{\partial y} = -\frac{2\nu_{ii}}{3\tau} (T_{\parallel} - T_{\perp}), \quad (3) \quad \frac{1}{\tau} \frac{dT_{\perp}}{dt} + \nabla_{\parallel} q_{\perp} + \left[\frac{\hat{\nabla}_{\perp}^2}{2} + \eta_{\perp} (1 + \hat{\nabla}_{\perp}^2)\right] \frac{\rho_s}{L_n} \frac{\partial \Psi}{\partial y} = \frac{\nu_{ii}}{3\tau} (T_{\parallel} - T_{\perp}), \quad (4)$$

where n is the ion density, u_{\parallel} is the ion velocity, T is the ion temperature, $\tau = T_{i0} / T_{e0}$, T_{i0} and T_{e0} are ion and electron temperatures at the plasma center, $\eta = L_n / L_T$, L_n is the density gradient length, L_T is the ion temperature gradient length, q is the heat flux, and ν_{ii} is the collision frequency between the ions. The subscripts \parallel and \perp represent the quantities in the parallel and perpendicular direction to the magnetic field, respectively. The time and spatial length are normalized with Ω_{ci} and ρ_s , where Ω_{ci} is the ion cyclotron frequency. Ψ is the gyro-averaged potential $\Psi \equiv \Gamma_0^{1/2} \Phi$, where $\Gamma_0^{1/2} = (1 - b\tau/2)^{-1}$ and $b = -\nabla_{\perp}^2$. Quantity b represents the magnitude of the FLR effect. The FLR effect is included in Ψ , $\hat{\nabla}_{\perp}^2$ and $\hat{\nabla}_{\perp}^4$ terms, where

$$\frac{\hat{\nabla}_{\perp}^2}{2} \Psi \equiv -\frac{b\tau/2}{(1+b\tau/2)} \Psi = \Psi_1, \quad (5) \quad \hat{\nabla}_{\perp}^4 \Psi \equiv 2\Psi_1 + \frac{b^2\tau^2/2}{(1+b\tau/2)^2} \Psi. \quad (6)$$

The quasi-neutrality relation is given to be

$$\Gamma_0 \left(n - \frac{b/2}{1+b\tau/2} T_{\perp} \right) - (1-\Gamma_0) \frac{\Psi}{\tau} = \Psi \quad (7)$$

to determine the relation between the density and potential. Collisions are dominant in this system, and higher order moments of the gyro-kinetic equation give simplified forms of the heat flux as follows:

$$q_{\parallel} = -\frac{3}{v_{ii}\tau} \nabla_{\parallel} T_{\parallel}, \quad q_{\perp} = -\frac{1}{v_{ii}\tau} \nabla_{\parallel} T_{\perp}. \quad (8) \quad (9)$$

2.2 Numerical Scheme

To obtain the linear eigen-mode and -frequency, a spectral code is developed. The Bessel expansion in the r direction and Fourier expansions in the θ, z directions are applied on Eqs. (1) - (4) and (7) by using

$$\phi(r, \theta, z) = \sum_{m=-M}^M \sum_{j=1}^J \sum_{l=1}^L \phi_{mj} J_m(\lambda_{mj} r/a) e^{im\theta} \cos\left(\frac{\pi}{2}(2l-1)z/L_z\right), \quad (10) \quad u_{\parallel}(r, \theta, z) = \sum_{m=-M}^M \sum_{j=1}^J \sum_{l=1}^L u_{\parallel mj} J_m(\lambda_{mj} r/a) e^{im\theta} \sin\left(\frac{\pi}{2}(2l-1)z/L_z\right). \quad (11)$$

Density n and temperature T are also expanded in the same way as in Eq. (11). The equations are solved in the region between $r = 0$ (center of the plasma) and $r = a$ (outer boundary of the plasma). The boundary condition in the radial direction are set to $f = 0$ at $r = 0, a$ when $m \neq 0$, and $\partial f / \partial r = 0$ at $r = 0, f = 0$ at $r = a$ when $m = 0$. Functions $J_m(\lambda_{mj} r/a)$ are used for the expansion to satisfy the boundary conditions, where $J_m(r)$ is the Bessel function, λ_{mj} is the j -th point with $J_m(\lambda_{mj}) = 0$, and m is the azimuthal mode-number. Periodic boundary conditions are used in the axial direction, and the effect of the end plate is not considered. We solve the matrix of the equations with the spectral expansion using the eigenvalue method. In the eigenvalue method, the eigenvalues of the matrix are obtained using the mathematic library MKL to give the linear growth rate.

For the linearization, the differential operator d/dt and ∇_{\parallel} are replaced to $i\omega$ and ik_z , where k_z is the wavenumber in the parallel direction. The real and imaginary part of ω give the frequency and growthrate, respectively. The axial mode number is set to l , which gives $k_z = 2\pi l \rho_s / L_z$, where L_z is the device length. In the local analysis in Ref. 13, the radial and azimuthal wavenumbers are assumed to be same to give $k_{\perp}^2 = 2k_0^2 = 2(m\rho_s/a)^2$, but in the global model k_{\perp} are given to be $\hat{\lambda}_{mj} = \lambda_{mj} \rho_s / a$ for function $J_m(\lambda_{mj} r/a)$.

2.3 Target Plasma

The geometry of the plasma is a simple cylindrical shape, and the magnetic field has only the axial component with a uniform intensity. For the simulations, experimental parameters in PANTA are used; device length $L_z = 4.0$ m, plasma radius $a = 0.07$ m, density $n_0 = 1.0 \times 10^{19} \text{ m}^{-3}$, $L_n = 0.07$ m, $v_{ii} = 350 \text{ s}^{-1}$, magnetic field $B = 0.1$ T, temperatures $T_{e0} = 3$ eV and $T_{i0} = 0.3$ eV. The temperatures and magnetic field give $\rho_s = 1.1$ cm, $\rho_i = 3.5$ mm and $\Omega_{ci}/2\pi = 3.8 \times 10^4$ Hz for argon plasmas. With these parameters, $\rho_i/L_n = 0.05 \ll 1.0$, $k_z \rho_i = 5.5 \times 10^{-3} \ll 1.0$ with $l = 1$ and $k_{\perp} \rho_i = 0.02 \ll 1.0$ with $m = 1$, so the gyro-kinetic ordering is satisfied. The other parameters for the analysis are τ and η_i .

3. Linear Instability

Numerical analyses are carried out using the developed gyro-fluid code. Figure 1 shows the dependences of the growthrate on the azimuthal and axial mode number. Here simplification with $\eta_{\parallel} = \eta_{\perp} (= \eta)$ is applied. The mode numbers of the most unstable modes in this parameter are $m = 2$ and $l = 1$. The critical value η_c of the instability in this condition is about 1.2, and the value of the growthrate increases as η increases. The global code can give the radial distribution of $T_{\perp}, T_{\parallel}, n, u_{\parallel}, \Phi$, and Ψ in addition to the growthrate and eigen-frequency. Figure 2 shows the radial profiles of $T_{\perp}, T_{\parallel}, n$ and u_{\parallel} with $m = 2, l = 1, \eta = 1.2$ and $\tau = 1$ of an argon plasma. The growthrate and frequency are given to be $\omega_i = 2.9 \times 10^{-3}$ and $\omega_r = -9.6 \times 10^{-3}$. Similar results were obtained by the analysis with the local model introducing the k_r value as a parameter.

The ion temperature is the most important parameter for the ITG instability, so the dependency on the magnitude and gradient length of the ion temperature is evaluated. Figure 3(a) shows the contour plot of the growthrate in the τ and η space. The critical value η_c for the ITG instability changes depending on the magnitude of τ . The minimum of η_c is $\eta_c = 0.8$, and increases as τ increases ($\eta_c = 1.7$, when $\tau = 2.0$, for example). These are the same tendencies as in the local model analyses as in Fig. 3(b). The cross in Fig. 3 indicates one of the experimental conditions in PANTA ($\tau = 0.1, \eta = 0.2$ with an argon plasma). It suggests that a higher temperature gradient is needed to observe the excitation of the ITG mode in PANTA.

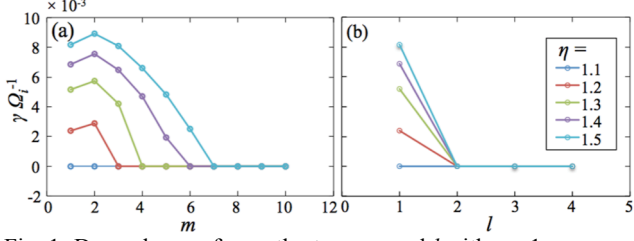


Fig. 1: Dependency of growthrate on m and l with $\tau = 1$, an argon plasma.

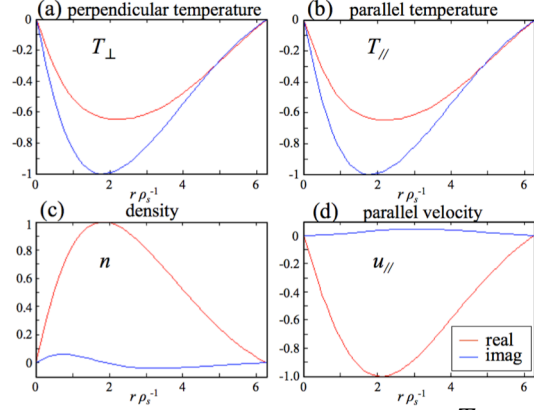


Fig. 2: Radial profiles of eigenmodes of (a) T_{\perp} , (b) T_{\parallel} , (c) n and (d) u_{\parallel} with $m = 2$, $l = 1$, $\eta = 1.2$, $\tau = 1$, an argon plasma.

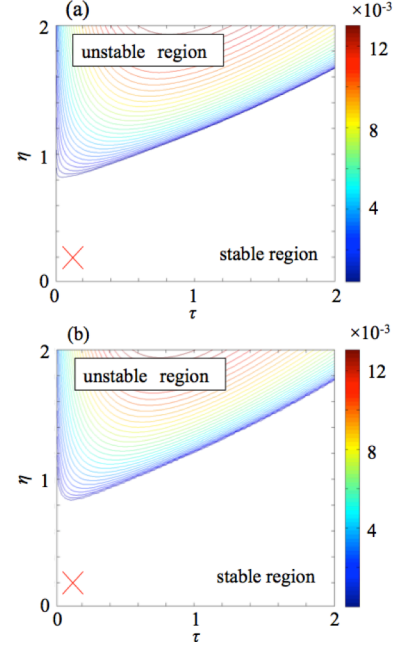


Fig. 3: Contour plot of the growthrate in the τ and η space with $m = 2$, $l = 1$, an argon plasma. The cases with the (a) global and (b) local analysis are plotted.

4. Parameter Dependency of Radial Structures

Dependencies on the other experimental parameters are also evaluated. The ion mass depends on the using discharge gas, which makes the Larmor radius different. The effective plasma radius changes, because the spatial length is normalized by the Larmor radius. Figure 4 shows the ion mass dependences of critical η_c with $m = 1-5$ in the cases with the global and local analyses. The cases of helium, neon, and argon discharges are plotted. The difference in the dependency on the mode number is partly due to the selection of k_r . In the global model, k_r of the most unstable mode is determined by calculating the eigenmode, though it is only a parameter in the local model. In the case with helium, as shown in Fig. 4, the m dependence is greatly different. The local analysis gives critical value $\eta_c = 1.9$, which is larger than that $\eta_c = 1.2$ in the case with the global analysis, when $m = 1$. This is because the value of k_{\perp} of the most unstable mode is larger than the value obtained from $k_r = k_0$ assumed in the local analysis. Figure 5 shows the relative amplitudes of the k_{\perp} components in the eigenmodes of the density. The maximum value is normalized to be the unity. $\hat{\lambda}_{mk}$ represents the normalized wave length of the base Bessel functions. As is seen in Fig. 5, there is a peak at $\hat{\lambda}_{mk} = 0.7$, but in the local analysis the smaller value $k_{\perp} = \sqrt{2}(2m/a)\rho_s = 0.14$ is used. Figure 5 also shows that the value of $\hat{\lambda}_{mk}$ giving the maximum amplitude is almost the same in spite of the ion mass variation.

In addition, the difference in the treatment of k_0 is the other cause. The value of k_0 is given as m/r , and is evaluated at one point, typically at $r = a/2$ in the local model. On the other hand, in the global model, since $1/r$ terms are expanded, so the following relation is used for the azimuthal derivative;

$$\frac{\partial}{\partial y} A_i = \langle ik_{\theta} A \rangle_i = i \sum_{k=1}^K \frac{2mA_k}{J_{m+1}^2(\lambda_{m,i})} \int_0^1 dr J_m(\lambda_{m,k} r_s) J_m(\lambda_{m,i} r_s). \quad (12)$$

This calculation gives connection between the various Bessel functions. The radial structure also affects the evaluation of k_0 . Figure 6 shows the radial profiles of the amplitudes of n when $m = 2$, $l = 1$, $\eta = 1.2$ and $\tau = 1$. In the case of helium, the structure localized near the center of the plasma is formed as compared with the cases of argon and neon. This is because the characteristic spatial scale ρ_s is changed. From this result, it is not appropriate under this condition to set the evaluation position at $r = a/2$ in the local analysis. Since the differences in the mode structures greatly affect the growth rates of the ITG instability in this way, it can be said that it is meaningful to analyze the detailed mode structures by the global analysis.

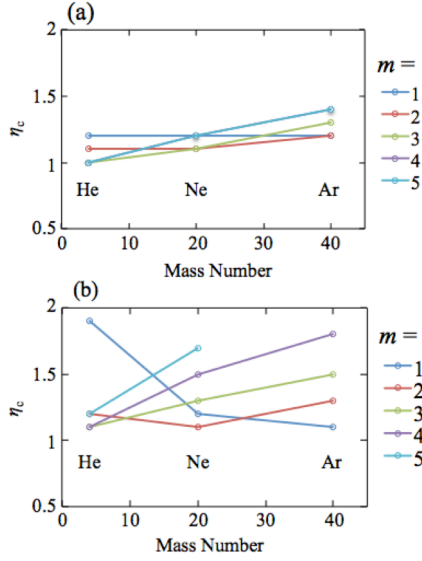


Fig. 4: Ion mass dependences of the critical value η_c , when $\tau = 1$. Those of modes with $m = 1 - 5$ are shown in the case with the (a) global and (b) local analyses.

5. Summary and Discussion

To investigate the excitation conditions of ITG modes in PANTA linear device, the linear instability analyses were carried out. A gyro-fluid code, which solves global eigen-functions including the FLR effect, was developed and used for the analysis. The same tendency from the local model was obtained, which gives the threshold for the instability in the linear device. Wavenumber k_{\perp} of the most unstable mode was obtained with the radial mode structure analysis. The radial structure is affected by the relative size between the plasma radius (to give the boundary condition) and the Larmor radius (to give the typical spatial length of the instability). The mode is more localized near the center of the plasmas in the case of a discharge gas with a smaller mass number as helium.

From the gyro-fluid model, it was found that the experimental parameters of PANTA are present in the stable region, and for excitation of the ITG instability 4 times or more larger η is required. In linear machine CLM, the ITG instability has been observed in the case when the radial positions of the steep temperature and density gradient are different from each other to satisfy the excitation condition on η [10]. The condition of destabilization should be explored by the distribution controls of the temperature and density in the future.

Acknowledgements

This work is supported by JSPS KAKENHI Grant Number JP16K06938, and the collaboration program of NIFS (NIFS17KNST112, NIFS16KNXN323) and RIAM of Kyushu University.

Reference

- [1] P.H. Diamond, *et al.*, Plasma Phys. Control. Fusion **47**, R35 (2005).
- [2] G. R. Tynan, A. Fujisawa and G. McKee, Plasma Phys. Control. Fusion **51**, 113001 (2009).
- [3] W. Horton, Rev. Mod. Phys. **71**, 735 (1999).
- [4] A.K. Sen, *et al.*, Phys. Rev. Lett. **66**, 429 (1991).
- [5] N. Ezumi, *et al.*, J. Nucl. Mater. **337**, 1106 (2005).
- [6] S. Inagaki, *et al.*, Sci. Repts. **6**, 22189 (2016).
- [7] Y. Miwa, *et al.*, Plasma Fusion Res. **8**, 2403133 (2013).
- [8] G. Hattori, *et al.*, Plasma Fusion Res. **10**, 3401060 (2015).
- [9] W. Dorland and W. Hammet, Phys. Fluids B **5**, 812 (1993).

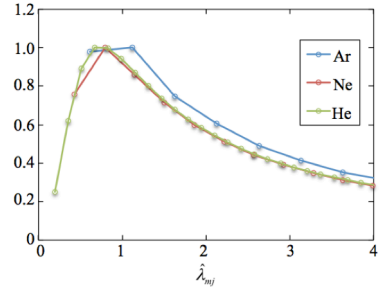


Fig. 5: Relative amplitudes of the k_{\perp} components in the eigenmodes of the density n , when $\tau = 1$, $\eta = 1.2$, $m = 1$ and $l = 1$. Dependences on $\hat{\lambda}_{mk}$, normalized wave length, are plotted.

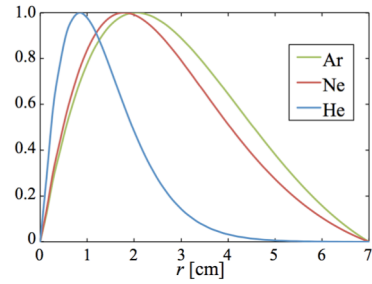


Fig. 6: Radial profiles of amplitudes of the density n with $m = 2$, $l = 1$, $\eta = 1.2$, $\tau = 1$.

磁場閉じ込めプラズマにおける主要素以外の効果に関する検討:

不純物と中性粒子

On Effects of Impurities and Neutrals in Magnetically Confined Plasmas

N. Kasuya¹, M. Yagi¹, A. Fukuyama², T. Ohno³, M. Sasaki, S. Abe³, T. Kobayashi⁴ and S. Inagaki

Research Institute for Applied Mechanics, Kyushu University, Kasuga, Fukuoka 816-8580, Japan

¹ National Institute for Quantum and Radiological Science and Technology, Obuchi, Rokkasho, Aomori 039-3212, Japan

² Department of Nuclear Engineering, Kyoto University, Kyoto 606-8501, Japan

³ Interdisciplinary Graduate School of Engineering Sciences, Kyushu University, Kasuga, Fukuoka 816-8580, Japan

⁴ National Institute for Fusion Science, Toki, Gifu 509-5292, Japan

E-mail: kasuya@riam.kyushu-u.ac.jp

Magnetically confined fusion plasmas consist of several elements. Not only main plasma but also their isotopes, impurities and even neutral particles are important players for the plasma confinement anywhere in the core, edge and SOL regions. These synergetic effects must be clarified. In this research, two kinds of topics are considered regarding this object: i) development of a simulation tool for investigating the impurity control in fusion reactor by using the integrated simulation code TASK, and ii) turbulence simulation taking account of inhomogeneity of neutral density in linear devices by using the resistive drift-wave turbulence code NLD.

The first topic is on the development of a simulation tool for investigating the impurity control. High Z impurities come from the vessel wall as tungsten used in ITER, so establishment of the control method is crucial for the plasma confinement. There are some experimental results that electron cyclotron resonant heating (ECH) is effective to spill out the accumulated impurities in the core region [1]. To clarify the appropriate condition for the impurity control, we are developing an integrated simulation code to evaluate transport of multi species ions in tokamaks. The transport code TASK/TR [2] is being modified for that purpose. To calculate transport of tungsten, atomic processes as ionization and recombination between multiple charge states must be considered. Near the center of plasma, where the plasma pressure gradient is rather small, the neoclassical transport process is the key to determine the impurity transport [3]. For the first step, response of the background plasmas is calculated by applying an additional ECH, whose power deposition position is localized near the plasma center. A monotonic response is obtained in accordance with the input power in the parameter region of the ASDEX experiment, which is possible to affect the impurity transport. In the present version of TASK/TR, several kinds of transport models are installed. For the neoclassical transport, Hinton-Hazeltine model [4], Chang-Hinton model [5], and NCLASS model [6] can be selected. Three cases using these models are compared, and show no qualitative difference.

The second topic is on the effect of inhomogeneity of neutral density in linear devices. It is important to consider combination of inhomogeneities, which drive and/or damp instabilities

in magnetized plasmas. Inhomogeneity of neutral particle density is taken into account for analyzing turbulent states in a simple cylindrical configuration by combining two kinds of simulations in this research. One is a simulation for 2-D profiles of neutral particles, and the other is that for resistive drift wave turbulence. Radial and axial profiles of neutral particles are calculated by the Monte Carlo method [7] with a configuration of linear device PANTA [8]. The ratio for ionization of neutral particles depends on the electron temperature, and the higher temperature in the operation range makes the neutral density smaller near the center of the plasma. Figure 1 shows the radial profile of the neutral density. Then the radial profile of the ion-neutral collision frequency ν_{in} is set by introducing these neutral density profiles into resistive drift wave turbulence simulations [9]. Smaller ion-neutral collision frequency makes the instabilities more unstable, and its inhomogeneity enhances mean electrostatic potential formation [10]. Figure 2 shows the dependency of the potential on the dip of the ν_{in} profile, where the values of ν_{in} at the center of the plasma is related to $(1 - d_1)$. The potential at $r = 0$ shows rapid increase when $d_1 < 0.5$ as the ν_{in} dip is increased. Plasma flows can be driven by turbulent stresses from excited modes in magnetized plasmas, and convective derivative nonlinearity generates the azimuthal flow near the center of the plasma in this case. The radial inhomogeneity of the neutral density affects azimuthal flow generation by changing the phase structure of the most unstable eigenmodes [11]. Eigenmode analyses show that the mode structure has a complex Bessel-type function shape in the central region of the plasma, and the imaginary part arises from the radial inhomogeneity of the damping term caused by ion-neutral collisions. The amplitude of turbulent stress is proportional to the inhomogeneity under a marginally stable condition. Two roles of the neutral particles on the turbulence, direct change of linear instabilities and formation of background flows, become clear. Global structural formation is also an important factor for determining the plasma turbulent state, and this result clearly shows that several kinds of radial background distributions, the plasma and neutral densities in this case, can influence the global structures.

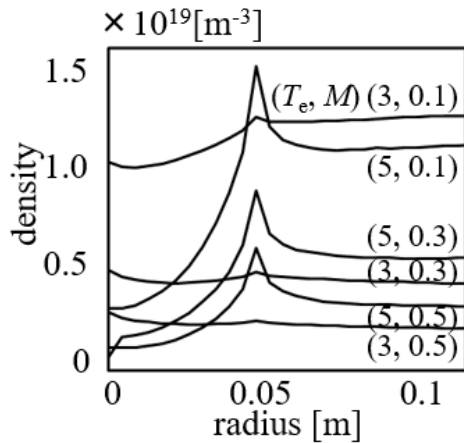


FIG. 1: Radial profiles of the neutral density, averaged in the axial direction. The cases with $T_e = 3, 5$ [eV] and $M = 0.1, 0.3, 0.5$ are shown.

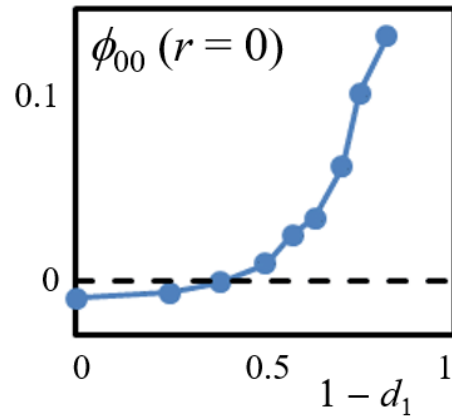


FIG. 2. Dependency on the ν_{in} dip of the formed potential at the plasma center ($r = 0$). d_1 represents the value of ν_{in} at $r = 0$ normalized with $\max(\nu_{in})$, and the spatially constant ν_{in} profile is given with $d_1 = 1$.

Acknowledgements

This work was partly performed under the Joint Special Design Team Collaborative Research Program (29K019), and was partly supported by JSPS KAKENHI Grant Number JP16K06938, by the collaboration program of NIFS (NIFS17KNST112, NIFS16KNXN323)

and RIAM of Kyushu University. Some numerical simulations were carried out on "Plasma Simulator" (FUJITSU FX100) of NIFS.

References

- [1] NEU, R., et al., Plasma Phys. Control. Fusion **44** (2002) 811.
- [2] FUKUYAMA, A., <http://bpsu.nucleng.kyoto-u.ac.jp/task/>.
- [3] ANGIONI, C. et al., Nucl. Fusion **54** (2014) 083028.
- [4] HINTON, F. L. and HAZELTINE, R. D., Rev. Mod. Phys. **48** (1976) 239.
- [5] CHANG, C. S. and HINTON, F. L., Phys. Fluids **29** (1986) 3314.
- [6] HOULBERG, W. A., et al., Phys Plasmas **4** (1997) 3230.
- [7] IGNATENKO, M., et al., Jpn. J. Appl. Phys. **46** (2007) 1680.
- [8] INAGAKI, S., et al., Sci. Rep. **6** (2016) 22189.
- [9] KASUYA, N., et al., Phys. Plasmas **15** (2008) 052302.
- [10] KASUYA, N., et al., Phys. Plasmas **25** (2018) 012314.
- [11] KASUYA, N., et al., J. Phys. Soc. Jpn. **87** (2018) 024501.

Simulation studies on transport of multi-species plasmas including impurity ion

Masanori Nunami

National Institute for Fusion Science, Toki 509-5292, Japan

Anomalous and neoclassical transport of multi-species plasmas including impurity ion are investigated by gyrokinetic and drift-kinetic simulations. In a high ion temperature plasmas heated by neutral beam injection in Large Helical Device, the gyrokinetic simulations indicate that the particle fluxes can be varied according to changes of plasma profiles and the constitution of particle species, and the turbulent contribution of the impurity particle flux remains radially inward directed within certain changes of the temperature gradients. On the other hand, the drift-kinetic simulations show that the neoclassical particle fluxes of ions can change due to generated radial electric field and the external momentum sources.

1 Introduction

In order to design the fusion reactors, the transport phenomena of plasma heat and particles should be accurately predicted by theoretical approaches, and numerical simulation approaches based on the kinetic frameworks are powerful for it. Simulation studies on the transport of the plasma consists of multi-ion-species are strongly needed to understand the physics of the burning plasma in the ITER, future reactors, and also the plasma in stellarators such as the Large Helical Device (LHD) [1], because there exists quite complicated transport properties through the multi-transport channels produced in the multi-species plasmas. In addition, in the multi-ion-species LHD plasmas heated by neutral beam injection (NBI), the extremely hollow impurity density profiles called *impurity hole* are often observed, and understandings of their generation mechanism is a critical issue for magnetically confined plasma researches. In such plasmas, the transport fluxes of heat and particles should be calculated by kinetic simulations for the neoclassical and anomalous contributions to the transport, where the transport should be determined by the total transport fluxes including the both contributions. In this work, we try to calculate the transport fluxes of multi-ion-species LHD plasmas with impurity hole structure by gyrokinetic and drift-kinetic simulations.

2 Turbulent transport

Turbulent transport has been considered to be one of the most critical issues in the magnetically confined plasmas researches. In recent our linear gyrokinetic analyses of the micro-instability in the LHD impurity hole plasma, which consists of four species (e, H, He, and C), it was found that the ion temperature gradient (ITG) mode is a dominant instability [2]. Here, we perform the nonlinear gyrokinetic turbulence simulations by the GKV code [3, 4] in order to evaluate turbulent contributions of the plasma transport. In Fig. 1, ITG-dependences of the turbulent contributions of the radial transport fluxes of the heat and particle for all species satisfying the ambipolar conditions. All heat fluxes are increased with increasing ITG, which is one of the typical characters of the ITG-driven turbulent transport. On the other hand, we find that the particle transport fluxes have quite different ITG-dependencies among different particle species. Furthermore, the impurity carbon particle flux remains the negative (radially inward directed) within wide ranges of the ion temperature gradients from their nominal values.

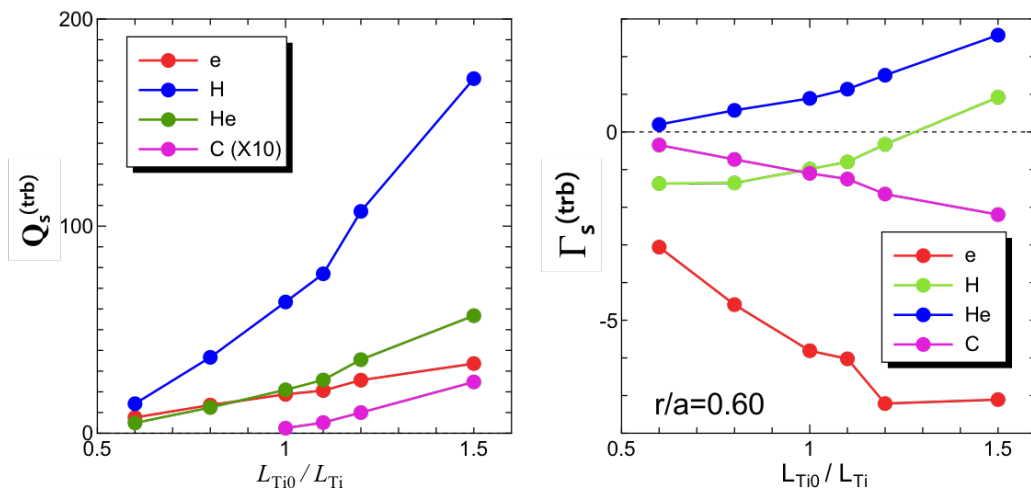


Fig. 1 GKV results for turbulent heat fluxes $Q_s^{(trb)}$ (left), and particle fluxes $\Gamma_s^{(trb)}$ (right) of each species as functions of the normalized ion temperature gradients ($L_{Ti} \equiv (-d \ln T_i / dr)^{-1}$) in the LHD impurity hole plasma. Here L_{Ti0} are nominal temperature gradient lengths of ion, and each fluxes are normalized by the arbitrary unit.

3 Neoclassical contributions

The neoclassical contributions of the transport of the LHD plasma are evaluated by using the DKES/PENTA code [5]. The code solves the drift-kinetic equation and evaluate the ambipolar radial electric field E_r . Since the neoclassical particle fluxes are quite sensitive to E_r and the external momentum torque by NBI heating. We evaluate the effects of the external torque

on the neoclassical fluxes, and it is found that the co-injected external torque can cause not only ion-root with negative E_r but also electron-root with positive E_r [6]. In the case of the electron-root, the neoclassical particle flux of carbon can be outward directed which is opposite directed to the turbulent fluxes. On the other hand, the ion-root E_r is often observed in the high- T_i LHD plasma [7], it should be discussed the possibilities of outward-directed neoclassical impurity carbon particle flux in the case of the ion-root. In the simulations performed here, we have not yet included other important effects, e.g., the poloidal variation of the electrostatic potential, and the direct contributions of the radial beam flux Γ_b to the ambi-polar condition. The studies on the neoclassical impurity particle flux with above effects will be performed as future works.

Acknowledgment

This work is supported in part by the RIAM collaborative Research Program (29FP-21), the Japanese Ministry of Education, Culture, Sports, Science, and Technology, Grant (26820398, 16K06941, 17K14899), NIFS collaborative Research Programs (KNST095, KNTT043, KNTT035), and the FLAGSHIP2020, MEXT within the priority study 6. The simulations are performed on "Plasma Simulator" (FUJITSU FX100) of NIFS.

- [1] Y. Takeiri, *et al.*, Nucl. Fusion **57**, 102023 (2017).
- [2] M. Nunami, *et al.*, 26th IAEA FEC, TH/P2-3 (2016).
- [3] T.-H. Watanabe and H. Sugama, Nucl. Fusion **46**, 24 (2006).
- [4] M. Nunami, T.-H. Watanabe, and H. Sugama, Plasma Fusion Res. **5**, 016 (2010).
- [5] D.A. Spong, Phys. Plasmas **12**, 056114 (2005).
- [6] M. Nunami, *et al.*, Plasma Fusion Res. **12**, 1203039 (2017).
- [7] T. Ido, *et al.*, Plasma Phys. Controlled Fusion **52**, 124025 (2010).

Simulation study on internal transport barrier formation using gyrofluid model(II)

M. Yagi, Y. W. Cho¹, H. Seto and T. S. Hahm¹

National Institutes for Quantum and Radiological Science and Technology,
Rokkasho Fusion Institute, Rokkasho, Aomori, Japan

¹Seoul National University, Seoul 151-744, Republic of Korea

1. Introduction

To understand physical mechanism of transport barrier formation is a crucial issue for designing advanced operation scenario in JT-60SA and ITER. In QST, the project for multi-scale simulation with transport/MHD is going on. On ITBTOK Project (IFERC-CSC), the quasi-linear modification of neoclassical flows is taken into account for GF-ITG code and we revisit the internal transport barrier (ITB) formation investigated by Tokunaga et al[1]. We report the recent simulation results on ITB formation by the improved transport model.

2. Model equations

GF-ITG code consists of three field equations (ion continuity equation, parallel momentum equation and ion temperature evolution equation)[1,2]. Here, we have improved ion temperature evolution equation as

$$\begin{aligned} \frac{3}{2}n_0(r)\left(\frac{dT}{dt} + \kappa_T \frac{1}{r} \frac{\partial \Phi}{\partial \vartheta}\right) - T_i(r)\left(\frac{dn}{dt} + \kappa_n \frac{1}{r} \frac{\partial \Phi}{\partial \vartheta}\right) = \\ \frac{5}{2\tau} \varepsilon \hat{\omega}_d T - \frac{9}{5\sqrt{\pi}} A |\nabla_{\parallel}| T + \frac{2}{5} A \nabla_{\parallel} V + \chi_{\perp} \nabla_{\perp}^2 T + S_T \end{aligned} \quad (1)$$

where the quasi-linear modification of ion temperature is taken into account, namely

$$T_i(r) = T_0(r) + \tilde{T}_{0,0}(r, t)$$

The Gaussian type of heat source is introduced as,

$$S_T(r) = P \exp(-(r - S_r)^2 / \Delta^2) \quad (2)$$

The total power is estimated by

$$P_T = 4\pi^2 R a^2 \int_0^1 r dr S_T(r) = VP \Delta^2 \left(\exp\left(-\frac{S_r^2}{\Delta^2}\right) - \exp\left(-\frac{(1-S_r)^2}{\Delta^2}\right) \right) + \frac{VPS_r \Delta^{(1-S_r)/\Delta}}{2} \int_{-S_r/\Delta}^{(1-S_r)/\Delta} \exp(-\xi^2) d\xi \quad (3)$$

where $V=2\pi^2Ra^2$ is the volume. For $S_r=0$, $\Delta=0.2$, $P_T=0.04VP$ and for $S_r=0.4$, $\Delta=0.05$, $P_T=0.0177VP$. In the following simulation, $P=10$, $S_r=0.4$, $\Delta=0.05$ are adopted.

3. Simulation results

Figure 1 shows mode spectrum in Fourier space (Type I). Here, resonant modes are located in the area where the relation $q_a < n / m < q_{\min}$ is satisfied. n is the toroidal mode number and m is the poloidal mode number. The safety factor profile q is shown in figure 2, where $q_a=3$, $q_{\min}=1.35$. The ion temperature profile and ion density profile are also shown. In Type I mode selection, low n off-resonant modes are also taken into account.

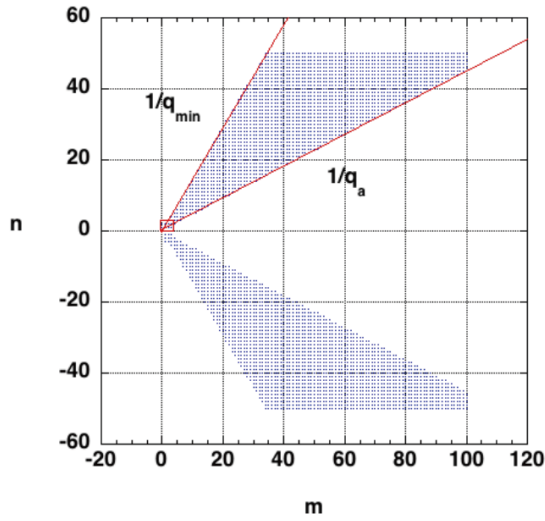


Fig.1 Mode spectrum in Fourier space (Type I).

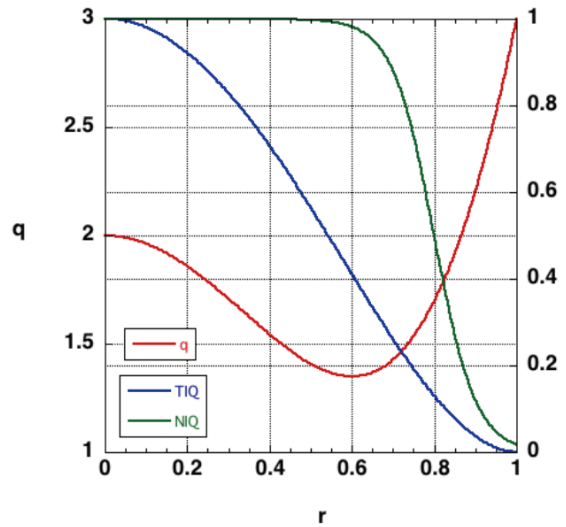


Fig.2 Safety factor profile, ion temperature profile and ion density profile.

Figure 3 shows temporal evolution of ion temperature profile. It is seen that clear ITB is not formed in this model with quasi-linear profile modification. The contour plot of fluctuating ion temperature at $t=20$ is shown figure 4. The strong convective transport is induced by the local heating.

Next, we investigate the effect of off-resonant modes on ITB formation. Figure 5 shows mode spectrum in Fourier space (Type II). The red dots show the resonant modes and low n off-resonant modes and blue dots show the medium and high n off-resonant modes. The ion temperature profiles for cases with Type I and Type II are shown in figure 6. It is found that these off-resonant modes weakly affect ion temperature profile evolution.

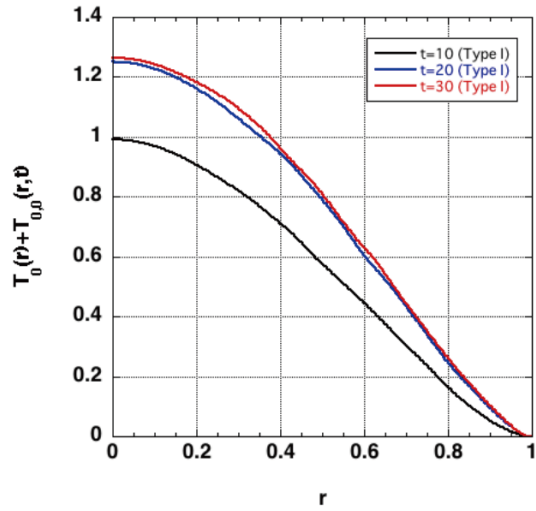


Fig.3 Temporal evolution of ion temperature profile.

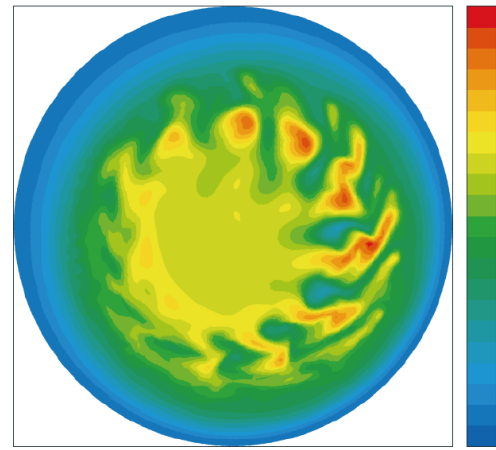


Fig.4 Contour plot of fluctuating ion temperature at t=20.

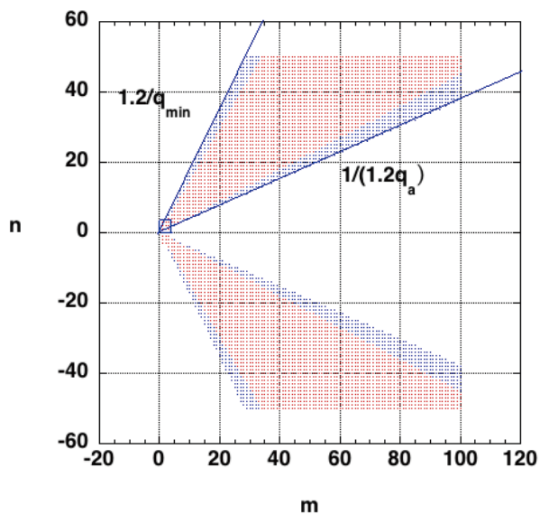


Fig.5 Mode spectrum in Fourier space (Type II).

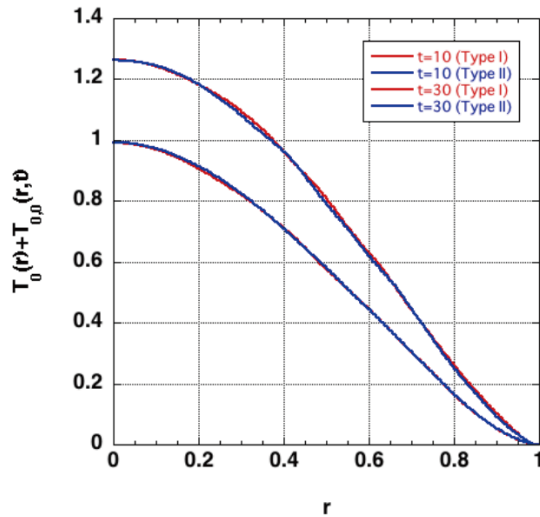


Fig.6 Comparison of ion temperature profiles for Type I and Type II mode selections.

4. Discussion

We have performed the flux driven simulation using gyro-fluid code taking account of the quasi-linear modification of ion temperature on ITB formation and investigate the time evolution of ion temperature profile using mode spectrum pattern Type I. It is found that this effect inhibits ITB formation. The effect of off-resonant modes on ITB formation is also investigated changing mode spectrum pattern. It is shown that Type II off-resonant modes very weakly affect ITB formation. Since quasi-linear modification of ion temperature profile

strongly affects ITB formation, so that we should carefully reconstruct ion transport equation as well as Shafranov shift effect. It is left as a future work.

Acknowledgments

The author would like to thank Drs. N. Miyato, A. Matsuyama and T. Takizuka for useful comments. The computation was carried out using the SELENE supercomputer system at IFERC-CSC.

References

- [1] S. Tokunaga et al., Nucl. Fusion 49 075023(2009).
- [2] M. Yagi et al., 14th BPSI meeting, RIAM, Kyushu Univ. (2016)
https://www.riam.kyushu-u.ac.jp/sosei/bpsi/2016/BPSI2016_proc.pdf